# Unraveling the Role of Carbon on the Strengthening Mechanisms of Low Mn-Si Martensitic Steels

*Master's Thesis*

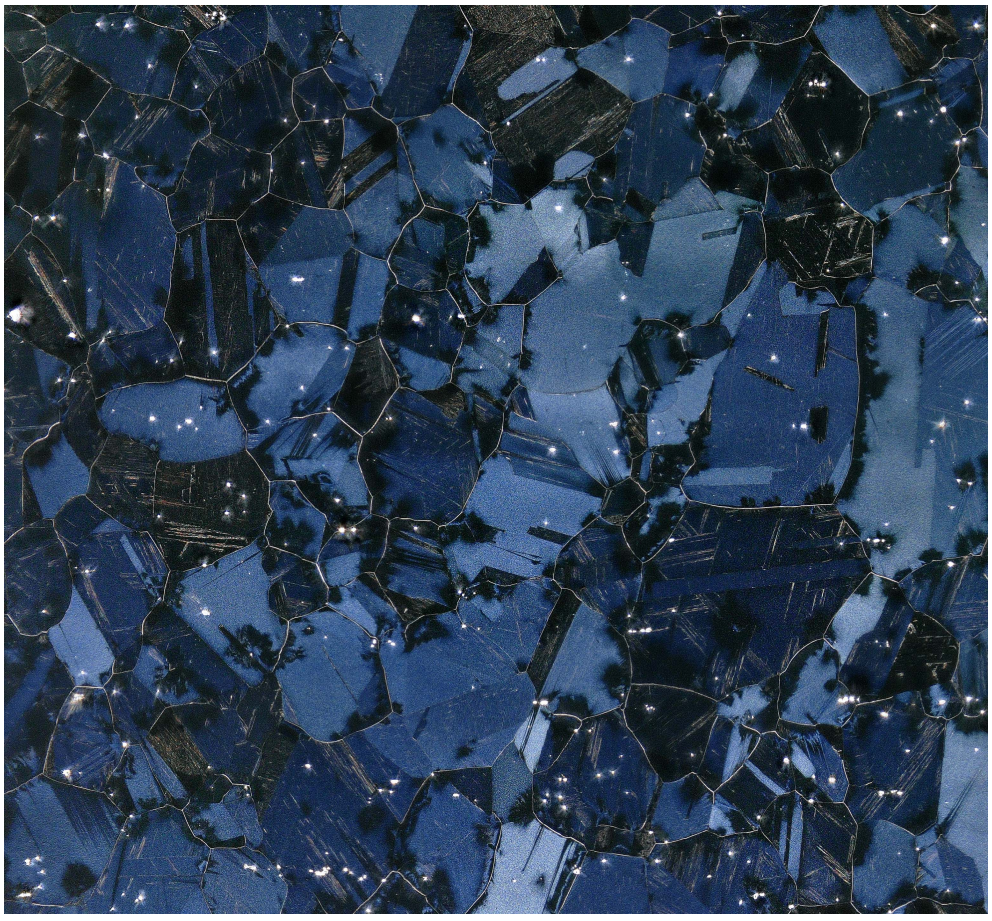

Vibhor Atreya

# Unraveling the Role of Carbon on the Strengthening Mechanisms of Low Mn-Si Martensitic Steels

THESIS

submitted in partial fulfillment of the
requirements for the degree of

MASTER OF SCIENCE

in

MECHANICAL ENGINEERING
TRACK MATERIALS ENGINEERING & APPLICATIONS

by

Vibhor Atreya
born in Meerut, India

Department of Materials Science & Engineering
Faculty Mechanical, Maritime & Materials Engineering
Delft University of Technology
Delft, the Netherlands

# Unraveling the Role of Carbon on the Strengthening Mechanisms of Low Mn-Si Martensitic Steels

Author: Vibhor Atreya
Student id: 4513088
Email: V.atreya@student.tudelft.nl

**Abstract**

The role of carbon in the strengthening mechanisms of martensitic steels has been studied for decades. However, uncertainties still exist regarding how the distribution of carbon to various locations inside martensite contributes to the development of its observed microstructure and high strength. The strengthening mechanisms depend on carbon content and process parameters, but are also inter-related. The current work is an attempt to address the existing uncertainties regarding the relation between martensite dislocation density ($\rho$), prior austenite grain size (PAGS) and the manner in which total carbon is distributed into martensite interstitial sites and segregations near dislocations. Two steel alloys with different carbon content were selected to study, having following composition in wt.%: 0.3C-3.6Mn-1.5Si and 0.6C-3.5Mn-1.5Si. Alloys were heat treated in dilatometer to obtain martensite with different prior austenite grain sizes (PAGS). Microstructure characterization was performed using X-Ray Diffraction (XRD), Scanning Electron Microscopy (SEM) & Electron back-scatter diffraction (EBSD) and strength was evaluated by hardness measurements. It was found that the main factor influencing the carbon distribution in martensite is the martensite dislocation density ($\rho$), but the magnitude of its influence depends upon PAGS and alloy composition. In 0.3 wt.% C alloy, $\rho$ decreases with increasing PAGS, as a result carbon atoms migrating towards dislocations during cooling also decrease, leaving higher number of carbon atoms at interstitial sites. However in 0.6 wt.% C alloy, such trend is not observed. On increasing the total carbon content in the alloy, very small increase in interstitial carbon content of martensite is observed if the PAGs are large. An increase in hardness was observed when the samples were introduced in liquid nitrogen, even in those cases where contribution from all strengthening mechanisms remained almost the same. This was unexpected and is most probably due to the relaxation of residual stresses and formations of carbon clusters at cryogenic temperature. In the end, an extension to already existing model is proposed to connect several microstructural features together in order to explain how they interact and evolve to give rise to observed strength of martensite.

Thesis Committee:

| | |
|---|---|
| Chair: | Assoc. Prof. Maria J. Santofimia, Faculty 3mE, TUDelft |
| University supervisor: | Dr. ir. Javier H. Garcia, Post-doc, Faculty 3mE, TUDelft |
| Committee Member: | Assoc. Prof. Amarante J. Böttger, Faculty 3mE, TUDelft |

# Acknowledgements

No task is a single man's effort. This project has been one of the most significant academic challenges I faced. Its completion would not have been possible without the help and support of many people, all of whose names cannot possibly be written down. I extend my honest appreciation to all of them. However, there are some people who were absolutely instrumental in bringing this project to fruition.

I would like to express my heartfelt gratitude to my supervisors: Dr. Maria J. Santofimia (Assoc. Prof.) and Dr. Javier H. Garcia (Post doc), who provided me the opportunity to work on this project. Both of them were constant source of guidance and motivation. During our bi-weekly meetings, Maria, through her challenging questions, always inspired me to have clarity and focus about my research goals. It was not easy for me in the beginning, and I often found myself struggling to find a direction. I am thankful to Javier, who in such situations, pointed me to correct resources and gave valuable suggestions so that I can find a way myself. I cherished working with both my supervisors.

I would like to thank all the laboratory in-charge for allowing me to conduct experiments and help me whenever possible. Valuable insight from other faculty members, post docs and PhD scholars during informal discussions also can not be underestimated. My friends and fellow master students helped me make this journey a fun filled and satisfying endeavor.

Special thanks to Dr M.P. Aarnts, Principle Researcher, Tata Steel, who agreed upon my request and provided to me valuable information for my report, by utilizing SEM and EBSD facilities at the company.

In the end, I thank my parents. It is because of them I am where I am. Their support and encouragement was worth much more than what can be expressed on paper.

Vibhor Atreya
Delft, the Netherlands
August 25, 2017

# Contents

# Chapter 1

# Introduction

Steel is an extra-ordinarily versatile material which finds usage in variety of industries such as construction, automotive, transportation, infrastructure, packaging, machinery and many more. It is primarily an alloy of iron and carbon in which several other constituents can also be present. History of steel goes back millenniums, but the modern era of steel started in mid-19th century [1]. Since then there have been rapid improvements in processes to improve both quality and quantity of steel produced. Over 75% of the steels in use today did not exist 20 years ago. Steel industry today is the second biggest industry in the world after oil and gas with an estimated global turnover of 900 billion USD and employing millions of people worldwide [2].

The use of steel is so widespread mainly due to its high strength and ductility. Steel with specific set of properties can also be developed according to the requirements. Today, there is an urgent need to develop efficient materials keeping in view the heightened awareness about environmental issues. For steel industry, this simply means low cost-lightweight steel with high strength which is easily recyclable. Therefore present-day steel research is mostly focused towards the same.

This work focuses on Martensite, which is the main strength contributing phase in a variety of steels [3]. Martensite possesses very high strength, but due to its complex microstructure, the understanding of strength contributions from different mechanisms operating inside martensite, is limited [4, 5]. This is because the microstructural features behind these strengthening mechanisms are inter-related and only few models exist which link them together. In this chapter, the reader is introduced first to martensite and other phases of steel, then to morphologies and complex microstructure of martensite and at last, research challenges, objectives and approach are described.

## 1.1 Steel: Composition and Phases

The major component of steel is iron (Fe) metal. Pure iron exhibits three kinds of allotropic crystal forms or phases, which exist at different temperature ranges: $\alpha$ iron (ferrite) exists up to 912 °C; $\gamma$ iron (austenite) exists between 912°C and 1394°C; and $\delta$ iron (delta ferrite) exists from 1394°C to melting point of pure iron, 1538 °C. Addi-

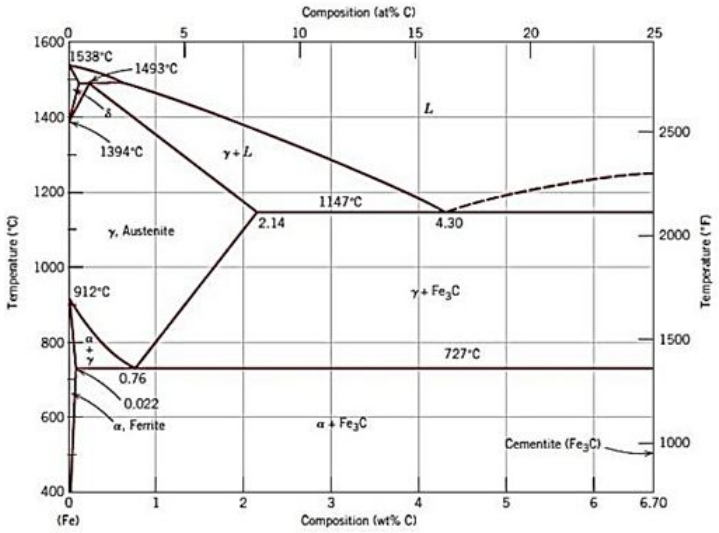


**Figure 1.1:** Fe-C Phase Diagram [6]

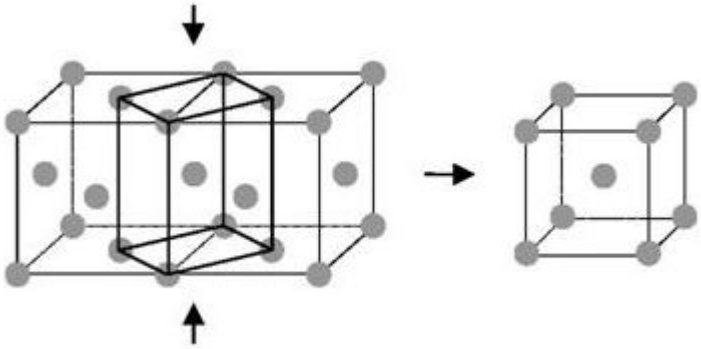

**Figure 1.2:** Two unit fcc cells with a smaller body centered tetragonal cell marked in the center (left). Under slow cooling, homogeneous compression in the direction of the arrows and an expansion in the plane normal to it occurs, and a bcc structure (right) is obtained [7]

tion of carbon or any other alloying element changes the range in which these phases are stable. Figure 1.1 is called a Fe-C phase diagram and depicts the changing temperature range with carbon concentration in which various phases of steel are stable. Different curves and their intersections in the diagram represent the condition in which two and more than two phases/mixture of phases co-exist in equilibrium respectively. This phase diagram is valid under a pressure of 1 atm. The phases depicted in it are formed at equilibrium conditions during very slow cooling of steel alloys. In reality, the cooling rates are high. Therefore, in such cases, the phase transformations do not take place at equilibrium, and some non-equilibrium phases are formed which do not appear in the phase diagram of figure 1.1.

## 1.2 Martensite

One of the most important non-equilibrium phase of steel is martensite. It is formed when steel in austenite phase is cooled rapidly to below a temperature called the martensite start ($M_s$) temperature. Below martensite finish ($M_F$) temperature, martensite transformation is considered complete. High cooling rates are required to form martensite. Austenite has a face centered cubic (FCC) structure with Fe atoms at corners & face center of unit cell, and C atoms occupying the interstitial sites at the edge centres. When steel is cooled from austenite phase sufficiently slowly, C atoms in austenite diffuse out, allowing a body centered cubic (BCC) ferrite phase to form which has Fe atoms at the corner and at the center of the unit cell with all the sides equal in length, shown in figure 1.2. But under rapid cooling, instead of a BCC structure, a body centered tetragonal (BCT) unit cell structure is formed which is called martensite. This is because under fast cooling, the C atoms do not have sufficient time to diffuse out of the austenite phase and the result can be thought of as a highly distorted BCC unit cell structure formed to accommodate excessive amount of C atoms trapped in the interstitial sites.

Since the martensitic transformation is not a diffusive one, the transformation of FCC austenite into BCT martensite occurs almost instantaneously. There is only a small displacement of individual atoms from their original position and large number of atoms experience a co-ordinated military type movement to form martensite. A unit cell of BCT crystal structure is like a BCC unit cell, which has been elongated along one of its dimensions, so that now the ratio of its height to the side of the base (known as $c/a$ ratio) is greater than 1. With increase in carbon concentration in alloy, the $c/a$ ratio (i.e, tetragonality) of the resultant martensite BCT structure increases.

### 1.2.1 Martensite Morphology

Martensite in steels exhibits four kinds of morphologies: laths, butterfly, lenticular(or plate) and thin plates [8]. There are several factors which decide the morphology including $M_S$ temperature, strength of austenite, critical resolved shear stress of slip and twinning, etc [9]. In general, two of the total four morphologies are most common: lath and plate. In alloys with less than 0.6 wt% C, martensite is formed as thin lath structures which are parallel to each other. A group of laths form larger entities called blocks, which further form packets together. This hierarchical structure is explained further in next section. In alloys with more than 1 wt% C, plate martensite is formed. It can be distinguished from lath martensite not only by its plate morphology but also by the presence of a central midrib. In between these two compositions, the microstructure exists as a mixture of the two morphologies [4]. The structural difference between them is that the lath martensite involves formation of dislocations, while plate martensite involves formation of twins [10]. Typical microstructures of lath and plate martensite are shown in Figure 1.3. Lath martensite exists in most commercial steels and is one of the main constituent of modern high strength alloy steels. Therefore, in this study, the focus is on lath martensitic microstructure.

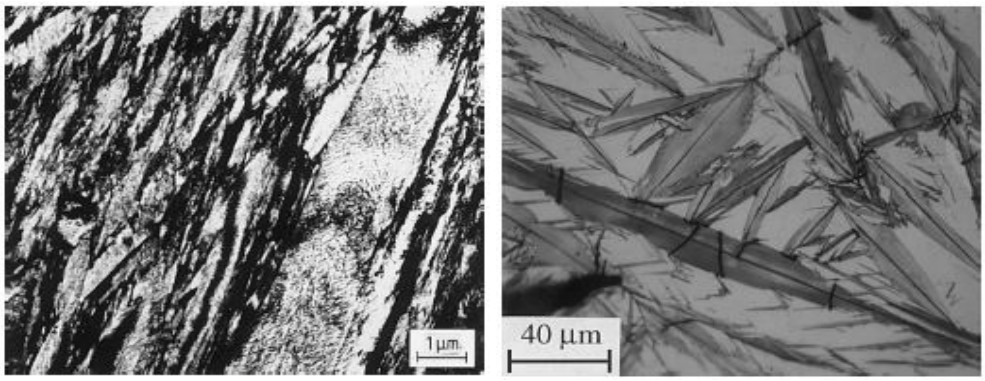


**(a)** Microstructure of Lath Martensite **(b)** Microstructure of Plate Martensite

**Figure 1.3:** Typical Martensite Morphologies [4]

### 1.2.2 Hierarchical Structure of Lath Martensite

The martensitic transformation is displacive and involves an invariant plane (also called the habit plane) which forms the interface of martensite and parent austenite grain [11]. There is a crystallographic relation that exists between the parent austenite phase and martensite at this interface. The Kurdjumov-Sachs (K-S) orientation relationship is one of them, which relates the (111) plane of fcc austenite ($\gamma$) to (011) plane of bct martensite ($\alpha$) and is written as:

$$(111)_\gamma||(011)_\alpha\ [\bar{1}01]_\gamma||[\overline{11}1]_\alpha \tag{1.1}$$

Because of symmetry, cubic systems have 24 equivalent crystallographic variants in martensite which can form from one single parent austenite grain [12]. The lath martensite units are very fine and each of them belong to one of these 24 variants. Laths tend to align themselves parallel to each other and form a 3-level hierarchical structure consisting of laths, blocks and packets as shown in figure 1.4. Individual laths have a misorientation of <5 deg in between them. A group of laths form a block. Blocks have a misorientation of 50 deg-60 deg. Group of blocks form a packet. Packets have a misorientation of 10 deg-20 deg or 47 deg-57 deg in between them [13]. A detailed analysis of this hierarchical structure can be found in [12].

## 1.3 Strengthening Mechanisms in Martensite

Several mechanisms contribute towards the overall strength of martensite. The yield strength of lath martensite, $\sigma_Y$ (in MPa), can be written as [14]:

$$\sigma_Y = \sigma_0 + \sigma_{ss} + \sigma_{gb} + \sqrt{\sigma_\rho^2 + \sigma_{pcpt}^2} \tag{1.2}$$

In the above equation, $\sigma_0$ = 50 MPa is the lattice friction stress for pure Fe and is a constant. $\sigma_{ss}$ is the contribution from solid solution strengthening, and is further

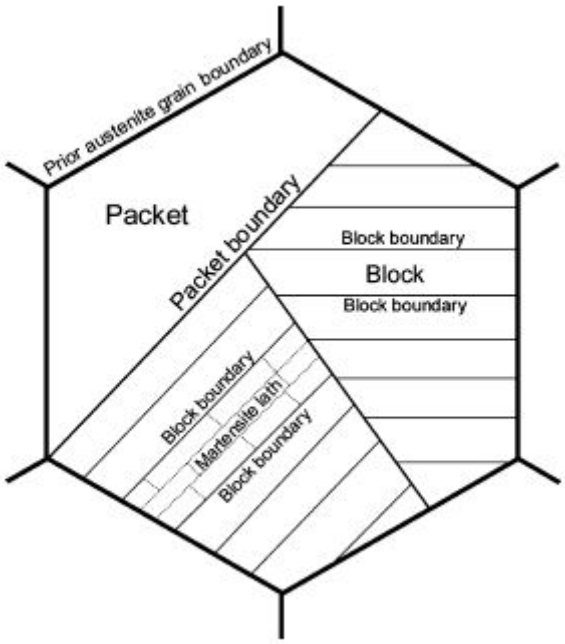


**Figure 1.4:** Hierarchical Microstructure in Lath Martensite [12]

subdivided as:

$$\sigma_{ss} = \sigma_c + \sigma_{st} \tag{1.3}$$

where $\sigma_c$ is contribution from interstitial carbon atoms and is calculated as:

$$\sigma_c = 1171.3 X_C^{1/3} \tag{1.4}$$

for untempered martensite, where $X_C$ is the average concentration of carbon in solid solution [14]. $\sigma_{st}$ is contribution from substitutional alloying atoms, and is given by:

$$\sigma_{st} = \sum_i (\beta_i^2 x_i)^{1/2} \tag{1.5}$$

where $x_i$ is the atom fraction of alloying element $i$ and $\beta_i$ is a constant accounting for the local modulus and lattice distortions of element $i$ with respect to pure iron [15]. $\sigma_{gb}$ is grain boundary strengthening and is attributed to block boundaries in martensite, as blocks are considered the best representation of a martensite grain [16]. The grain boundary strengthening is based on Hall-Petch relation [17] and is calculated as:

$$\sigma_{gb} = \frac{k_{HP}}{\sqrt{d_{block}}} \tag{1.6}$$

where $d_{block}$ is block width and $k_{HP}$ is Hall-Petch constant. $\sigma_\rho$ is the strength contribution from dislocations, and is calculated using Taylor equation:

$$\sigma_\rho = \alpha M G b \sqrt{\rho} \tag{1.7}$$

where $\alpha$, *M, G, b* and $\rho$, are geometrical constant, Taylor factor, shear modulus of material, magnitude of Burgers vector and dislocation density respectively [14]. $\sigma_{pcpt}$ is the applied stress required by dislocations to move past fine carbides and is determined by Orowan-Ashby equation [18] as:

$$\sigma_{pcpt} = \left(\frac{0.538 G b \sqrt{V_f}}{X}\right) ln\left(\frac{X}{2b}\right) \tag{1.8}$$

where $G$ is the shear modulus, $b$ is the Burgers vector, $V_f$ and $X$ are the volume fraction and diameter of carbide particles respectively. The Vickers hardness, $H_v$, can be written as a linear function of yield strength as [15]:

$$H_v = 0.4(\sigma_Y + 110) \tag{1.9}$$

## 1.4 Uncertainties in explanation of Martensite Strength

**Difficulties in studying martensite:** Due to complex hiearchial structure of martensite, it is difficult to know the accurate contribution of individual strengthening mechanisms on its overall mechanical strength. This is because in order to study the effect of a single strengthening mechanism, the contribution from other strengthening mechanisms should remain practically constant. This is difficult to achieve because the microstructural features of martensite, and therefore the strengthening mechanisms are inter-related. There will always be variations in more than one strengthening mechanisms, however controlled the thermal processing is [19]. So every strengthening mechanism has a direct effect on total strength, but also causes an indirect effect by affecting other strengthening mechanisms. Thus, simple addition of various strength contributions, such as in equation 1.2, is convenient for explanation of total strength on the basis of observed microstructural features, but is not adequate for accurate prediction of strength on the basis of composition and process parameters alone.

**Earlier investigations of inter-relation between martensite dislocation density, PAGS and total carbon content:** The martensite strength varies in proportion to the square root of carbon content [4]. Till early 1960's, this relationship was explained for as-quenched martensite in terms of solid solution strengthening due to interstitial carbon atoms [20]. But later it was found in some studies that the amount of carbon in true interstitials varied insignificantly with total carbon content [20, 5]. In figure 1.5, variation in internal friction with total carbon concentration for high purity Fe-C alloys is shown. Internal friction represents carbon concentration in interstitials. It can be seen that even when total carbon concentration increases by a factor of 10, internal friction

increases by a factor of less than 2. This, according to authors in [20], point to the fact that increase in interstitial carbon content is small when total carbon content increases. In figure 1.6, it can be seen that carbon concentration in interstitials is minuscule and shows no trend when compared to total carbon content. Above instances show that the majority of carbon atoms do not reside in interstitial sites and therefore, interstitial solid solution strengthening is not a complete explanation for contribution of carbon atoms to martensite strength. The carbon atoms which are not present at the interstitials sites were then believed to affect some other other strengthening mechanisms, resulting in increased strength. It was known that dislocation density of martensite increases with overall carbon content, and thus it was thought that it must be the segregated carbon atoms which are somehow related to this increase in dislocation density [20].

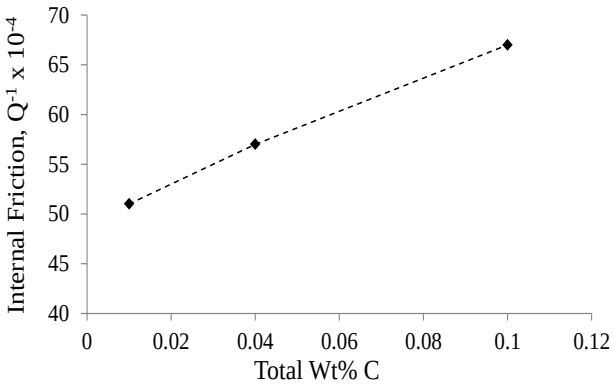


**Figure 1.5:** Variation in internal friction vs total carbon content [20]

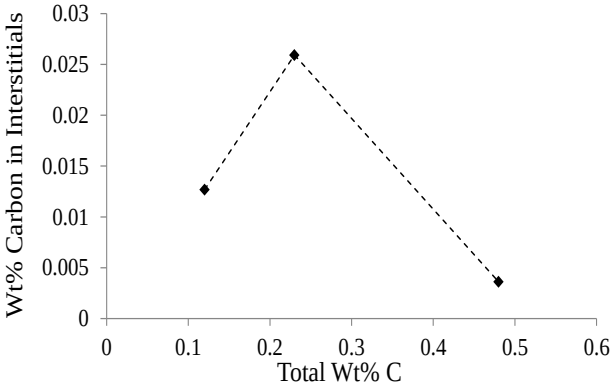


**Figure 1.6:** Variation of carbon content in interstitials vs total carbon content [5]

In another research, the authors show that the interstitial carbon content increases with increasing austenitizing time and temperature for medium carbon as-quenched martensite [21]. This can be seen in figure 1.7 where the magnitudes of two internal friction peaks correspond to dislocation density and carbon concentration in interstitials. The horizontal axis labels denote the austinitizing temperature and time in Kelvin and minutes respectively. Increasing austinitizing temperature and time would result in

larger PAGS. Therefore, it can be concluded that carbon concentration at interstitials increases with increasing PAGS. Dislocation density follows the same trend, although not very strictly. The drawback of this study is that too few cases are considered to make any general comments about observed trends. On the contrary, in [13], the authors observe that both interstitial carbon content and dislocation density decrease with increasing PAGS as shown in figure 1.8.

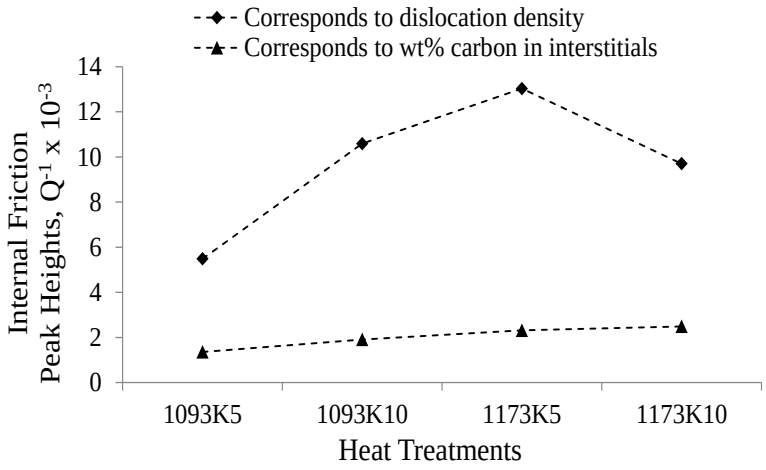


**Figure 1.7:** Magnitude of internal friction peaks for as-quenched martensites of a medium carbon steel. On horizontal axis, first four digits are austenitization temperature in K, while last digits are austenitizing time in min [21]

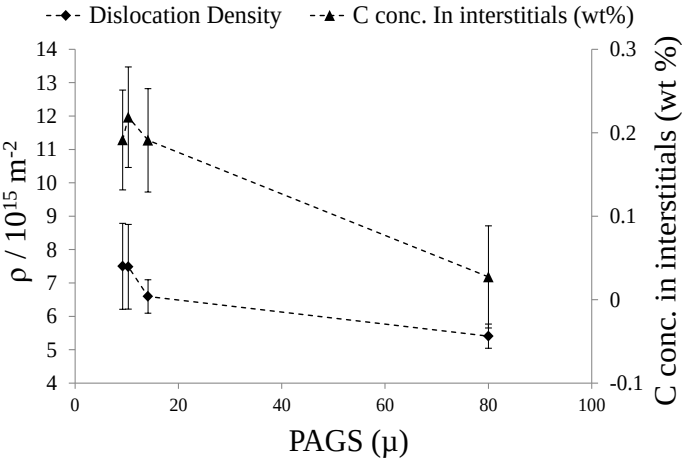


**Figure 1.8:** Variation of dislocation density and interstitial carbon content with PAGS in [13]

Above discussion proves the existing ambiguity regarding carbon distribution inside martensite and its relation with dislocation density. When the total carbon content is increased, dislocation density increases but interstitial carbon content does not increase much. And when PAGS is varied, dislocation density and interstitial carbon content both vary but it is still not clear how. It is expected that martensite dislocation density would follow a decreasing trend with increasing PAGS, since austenite matrix

is weaker at higher PAGS and would offer less resistance to plastic deformation during martensitic transformation [22].

**Hardness vs PAGS: Conflicting trends in literature:** Another point of confusion is the relation between hardness and PAGS in martensite. For this, it is important to define what can be considered as a grain in martensite. In [16], it is shown that a block is the best representative of a grain, and that the block size and flow stress follow Hall-Petch type relationship. The block size is also linearly dependent on prior austenite grain size (PAGS), so ultimately PAGS can also be used as an indicator of grain size. Therefore, a Hall-Petch type relationship between PAGS and martensite hardness is expected. Figure 1.9 shows variation of hardness with PAGS in different research. Hall-Petch relation is followed in [23, 24, 13, 25], but in some other research, the hardness seem to be unaffected by PAGS [5, 26] or it increases with increasing PAGS [27]. On some occasions both the behaviors were observed [21, 28]. In [27, 28], the departure from expected behavior is explained on the basis of role of the precipitates. In [21], it is explained on the basis of increasing amount of interstitial carbon with grain size. A detailed study of contribution from all the factors influencing hardness in as-quenched martensite in a larger range of PAGS is still missing.

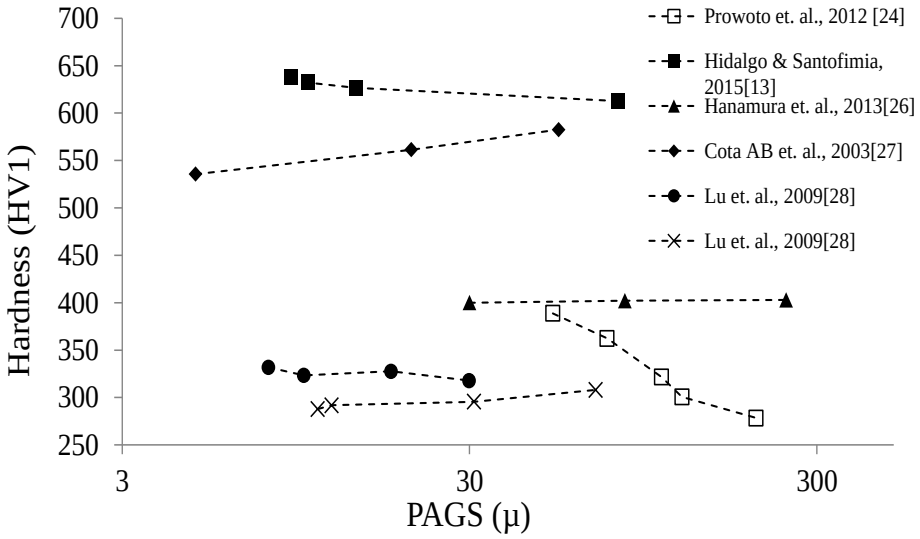


**Figure 1.9:** Variation of martensite hardness with PAGS in various research: Hidalgo & Santofimia, 2015 [13]; Cota AB et. al., 2003 [27]; Hanamura et. al., 2013 [26]; Prowoto et. al., 2012 [24]; Lu et. al, 2009 [28]

## 1.5 Martensite Dislocation Density as a function of Carbon in Solid Solution

In [29], authors developed a phenomenological model linking the changes in dislocation density and lath width of martensite with varying total carbon content in the alloy. The salient assumptions which were made for developing this model are:

- Full martensitic transformation has taken place at room temperature after quenching
- Complete carbon redistribution takes place from lath interiors towards dislocations at lath boundaries, forming cottrell atmospheres
- Simple shapes for martensite sub structures are considered: prismatic prior-austenite grains with hexagonal shape, packets of polygonal shape, and rectangular blocks and laths.

According to the model, the dislocation density, $\rho$, is given as:

$$\rho = \frac{3E}{(1+2\nu^2)\mu}\frac{4\varepsilon^2 d_{cottrell}}{d_{lath}^2 b} \tag{1.10}$$

where $E$ is the Young's Modulus, $\nu$ is poisson's ration, $\mu$ is the shear modulus and $b$ is the magnitude of burger's vector. $\varepsilon$ is the root mean square of lattice strain induced on each lattice direction from FCC to martensitic structure. $d_{cottrell}$ and $d_{lath}$ are the widths of cottrell atmosphere and martensite laths respectively, and are related as:

$$d_{lath} = \frac{d_{cottrell}}{(x_c^{\alpha'})^{2/3}} \tag{1.11}$$

where $x_c^{\alpha'}$ is the carbon atom fraction in the martensite structure available for segregation to dislocations and is calculated as:

$$x_c^{\alpha'} = x_{c,tot}^{\alpha'} - x_{c,ppt}^{\alpha'} \tag{1.12}$$

where $x_{c,tot}^{\alpha'}$ and $x_{c,ppt}^{\alpha'}$ are total carbon content and carbon content in precipitates respectively. After rearranging terms and incorporating equation (1.11), equation (1.10) can be written as:

$$\rho = \frac{3E}{(1+2\nu^2)\mu}\frac{4\varepsilon^2 (x_c^{\alpha'})^{2/3}}{d_{lath} b} \tag{1.13}$$

As total carbon content increases, $x_c^{\alpha'}$ increases and $d_{lath}$ decreases, resulting in an increase in $\rho$. This model also shows good agreement with the experimentally obtained trends. Although the model predicts the variation of dislocation density with varying total carbon content in martensite but it does not explain its variation with PAGS. An addition in this model will be suggested in chapter 4, in order to link $\rho$, PAGS and total carbon content together.

## 1.6 Research Objectives

In above discussion, some ambiguities in literature have been identified. This work attempts to resolve them by working towards following objectives:

1. To understand the distribution of total carbon content into true interstitial sites and segregation sites at dislocations under various conditions such as varying total carbon content and PAGS of martensite

2. To find out whether this distribution of carbon is related to observed dislocation density in martensite

3. To explain the observed variation in hardness of as-quenched martensite for different PAGS and carbon contents on the basis of contribution from different strengthening mechanisms

## 1.7 Approach

Two alloys with different carbon content 0.29C-3.58Mn-1.49Si and 0.57C-3.5Mn-1.5Si are selected for the study. As can be seen, they differ only in their carbon content. Several heat treatments are carried out to obtain as-quenched martensite samples with various prior austenite grain sizes (PAGS) for each alloy. Microstructure characterization for all the samples is carried out using techniques such as Optical Microscopy, X-Ray Diffraction (XRD), Electron Back Scatter Diffraction (EBSD) and Scanning Electron Microscopy (SEM). These techniques give information about PAGS, block sizes, dislocation densities, carbon in interstitials, fraction retained austenite and precipitate formation. Hardness measurements are carried out by Vickers Hardness Test Method. In the end, answer to research questions are stated on the basis of observed experimental results.

# Chapter 2

# Materials and Methods

This chapter describes the materials as well as experimental and theoretical procedures used in this study.

## 2.1 Initial Materials & Microstructures

The material studied are medium carbon steel alloys with composition as shown in Table 2.1. The alloys are denoted as LC or HC, depending upon carbon content. Samples with dimensions 2 mm x 4 mm x 10 mm were cut from large rolled sheets of raw material by electro-discharge machining (EDM), such that the longer dimension is parallel to rolling direction. To observe the initial microstructures, the samples were ground and polished using SiC abrasive papers of increasing grit number and in the final step using 1 micron diamond paste. Samples were etched using 2% Nital solution for 5-10 seconds and then observed under the optical microscope. Microstructure consisting of martensite laths is visible after etching in both alloys as seen in figure 2.1.

## 2.2 Dilatometry

For carrying out heat treatments, the initial samples were again ground and polished after recording their microstructure. A Bahr DIL 805 A/D dilatometer was used to carry out heat treatments. Dilatometry is a technique where change in length of a specimen is measured under controlled heating. Figure 2.2 shows different components of the dilatometer. It consists of a push rod made up of quartz, which is connected to a linear variable differential transformer (LVDT) on one side, and on the other side, it is in close contact with the sample material to register any change in length during heating or cooling of the sample. The LVDT has an accuracy of 1 $\mu$. The sample (with dimension 2 mm x 4 mm x 10 mm in current work) is placed in the space provided in the

| Steel | C | Mn | Si | Fe |
|---|---|---|---|---|
| LC | 0.29 | 3.58 | 1.49 | 94.64 |
| HC | 0.57 | 3.5 | 1.5 | 94.43 |

**Table 2.1:** Alloy Compositions in Wt%

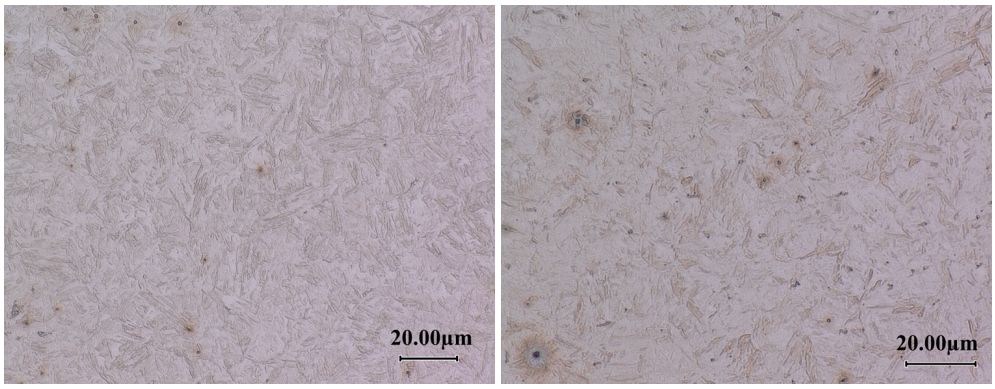


**(a)** Optical Micrograph of LC Alloy **(b)** Optical Micrograph of HC Alloy

**Figure 2.1:** Optical micrographs of LC and HC alloys

push rod. The space is adjustable. The sample is then moved under the induction coil which provides the required heating. Cooling of the sample is provided by blowing He gas at 5 bar pressure. Extent of heating or cooling is controlled by the software program with parameters provided by the user.

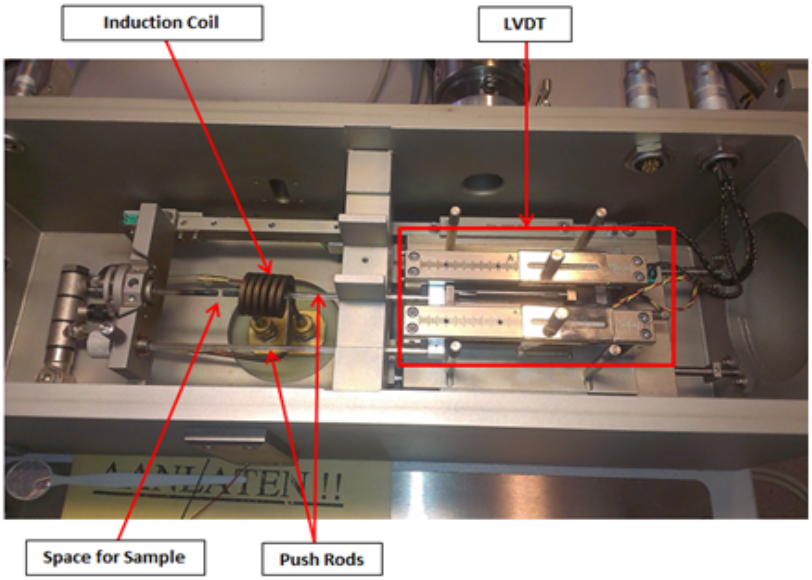


**Figure 2.2:** Components inside dilatometer

## 2.3 Thermal Etching

In order to reveal prior austenitic grain (PAG) boundaries, the samples were polished down to $1\mu$ in order to thermally etch them during heat treatments. Thermal etching involves preferential transfer of material away from grain boundaries when the steel is exposed to a high temperature in an inert atmosphere, as shown in figure 2.3. Because of this, grooves are formed which remain intact even after cooling. They are clearly

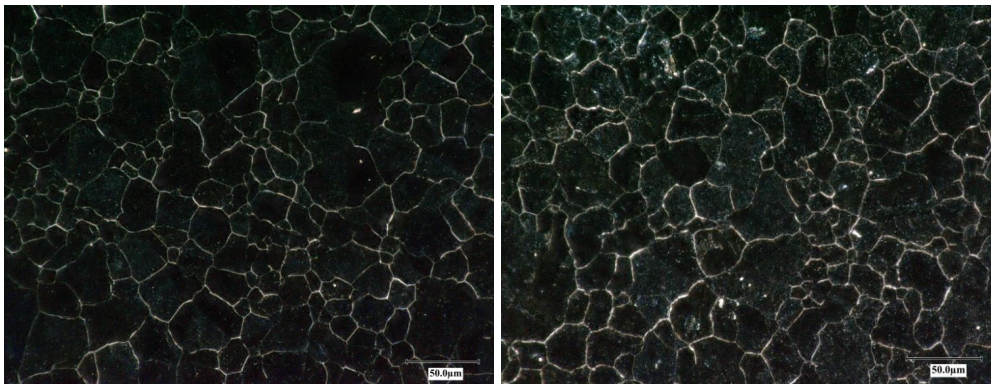


**(a)** Thermally Etched LC Sample **(b)** Thermally Etched HC Sample

**Figure 2.4:** Optical micrographs of thermally etched LC and HC alloys using partial illumination technique. The prior austenitic grain boundaries are visible

visible at room temperature outlining the austenite grain boundaries [30]. Thus, PAG sizes were measured using optical images of thermally etched samples (see Figure 2.4).

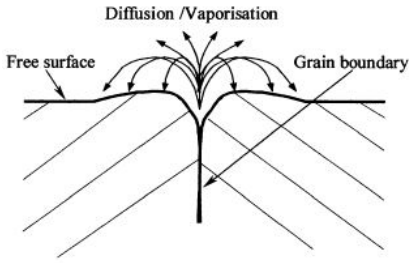


**Figure 2.3:** Groove formed at the intersection of a free surface with a grain boundary [30]

## 2.4 SEM Imaging and EBSD Measurements

After heat treatment in dilatometer, all samples were again ground & polished using SiC abrasive papers to obtain mirror finish, and with 1 micron diamond paste in the last step. For SEM, samples were lightly etched using 2% Nital solution, and then images were captured using Zeiss Ultra 55 machine equipped with a Field Emission Gun (FEG-SEM). The Electron Backscatter Diffraction (EBSD) system available on the machine was Edax Pegasus XM 4 Hikari EBSD system. EBSD scans used in this report were made on area of 50 micron x 50 micron, with step size of 100 nm.

### 2.4.1 Calculation of Block Width from EBSD Misorientation Profiles

Block widths were calculated by drawing multiple misorientation profile lines across several groups of parallel blocks. A representative line profile is shown in figure 2.5. Using the fact that block boundaries have a misorientation greater than 10 deg [13], average block widths were calculated. More than 100 blocks were considered for

calculating the average. An example of how the block width is calculated from a misorientation profile is shown in figure 2.6.

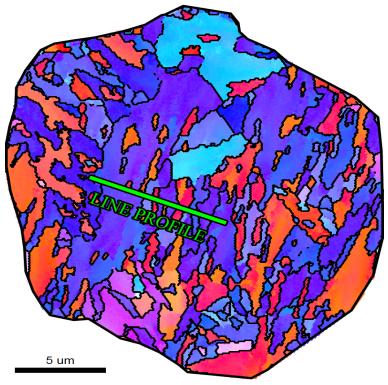


**Figure 2.5:** A misorientation line profile for measuring block widths from EBSD data

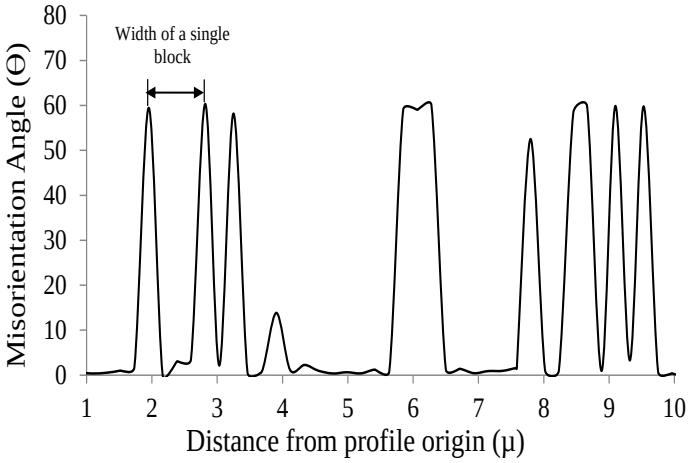


**Figure 2.6:** Calculation of block widths from misorientation profile

## 2.5 X-Ray Diffraction Experiments

For XRD, all heat treated samples were polished using SiC abrasive papers to obtain mirror finish, and with 1 micron diamond paste in the last step. They were further polished with 0.5$\mu$ OPS suspension for 10 min. The experiments were performed using Bruker D8 Advance diffractometer in Bragg-Brentano geometry and a Lynxeye position sensitive detector using Cu radiation. Measurements were performed using variable step sizes in three angular 2$\theta$ regions: 38 deg to 73 deg with a step size of 0.01, 73 deg to 109 deg with a step size of 0.017 and from 109 deg to 145 deg with a step size of 0.024. The base line of the XRD profile was removed and $K\alpha_2$ elimination was performed.

### 2.5.1 Dislocation Density Estimation using Modified Williamson-Hall Method

The broadening of XRD peaks is caused by small crystal size effect and lattice microstrains due to dislocations [31]. Therefore the peak broadening can be used to calculate dislocation density. For isotropic materials, this can be done by applying the Williamson-Hall equation [14]:

$$\Delta K \cong \frac{\alpha_s}{D} + Nb\sqrt{\rho}K \tag{2.1}$$

where $\Delta K$ is peak width, $\alpha_s$ is shape factor, $D$ is the crytallite size, $N$ is a constant, $b$ is the magnitude of Burgers vector, $\rho$ is the dislocation density and $K$ is the magnitude of diffraction vector which is calculated as $K = 2\sin\theta/\lambda$ [14]. But in case of strain anisotropy, which is observed in various real life materials including lath martensite, $\Delta K$ is not a linear function of $K$. In such cases, a modified Williamson-Hall equation is employed [14, 32]:

$$\Delta K \cong \frac{0.9}{D} + bM\sqrt{\frac{\pi}{2}\rho}(K\overline{C}^{0.5}) \tag{2.2}$$

where $M$ is a dimensionless constant called the dislocation distribution parameter. $\overline{C}$ is the dislocation contrast factor which accounts for the strain anisotropy. This equation gives $\Delta K$ as a linear function of $K\overline{C}^{0.5}$. $\overline{C}$ can be calculated as:

$$\overline{C} = \overline{C}_{h00}(1 - qH^2) \tag{2.3}$$

where $\overline{C}_{h00}$ is the average dislocation contrast factor for (h00) reflections, $q$ is a parameter that depends on edge or screw nature of the dislocations and $H = \frac{h^2l^2+l^2k^2+k^2h^2}{(h^2+k^2+l^2)^2}$ for every (hkl) reflection. Putting equation 2.3 into equation 2.2 we get:

$$\frac{(\Delta K - \alpha)^2}{K^2} \cong \beta^2\overline{C}_{h00}(1 - qH^2) \tag{2.4}$$

where $\alpha = \frac{0.9}{D}$ and $\beta = bM\sqrt{\frac{\pi\rho}{2}}$. $\alpha$ is chosen to get a best fit linear relation between $\frac{(\Delta K-\alpha)^2}{K^2}$ and $H^2$. From the graph 2.7a, $q$ can be obtained as the inverse of the intercept on horizontal axis. Theoretical values of $C_{h00}$ and $q$ for pure edge and screw dislocations can be calculated using elastic constants of the material $C_{11}$, $C_{12}$, $C_{44}$ and using [33]. Fraction of edge and screw dislocation can then be found out as:

$$f^{edge} = \frac{q_{screw} - q}{q_{screw} - q_{edge}} = 1 - f^{screw} \tag{2.5}$$

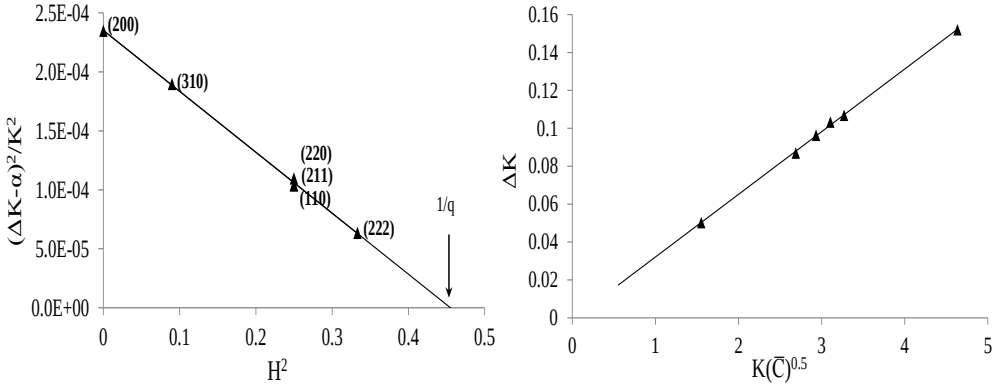


**(a)** $\frac{(\Delta K-\alpha)^2}{K^2}$ *vs* $H^2$ plot for a LC sample **(b)** $\Delta K$ vs $K\overline{C}^{0.5}$ plot for a LC sample

**Figure 2.7:** Peak widths $(\Delta K)$ plotted as function of different parameters for a representative LC sample. Number in the brackets denote miller indices of the diffraction planes.

where $f^{screw}$ and $f^{edge}$ are the fraction of screw and edge dislocations in the material respectively. From these fractions, and from $C_{h00}$ values for pure edge and screw dislocations, the average dislocation contrast factor for (h00) reflection, $\overline{C}_{h00}$, can be calculated. The final step is to plug in all the values into equation 2.2 for every peak and plot a straight line curve as shown in the Figure 2.7b. ρ can then be calculated using slope of this line and equation 2.2. The values of different parameters used in equation 2.2 are M = 1.2 and b = 0.286 nm [14] and elastic constants for LC [14] and HC [34] alloy taken from literature to be equal to elastic constants of alloys with similar carbon content.

In order to calculate the peak width from XRD diffractographs, all the peaks were well fitted with Voight function, which is a convolution of Gaussian and Lorentzian functions. The fitting was done using Origin software and the information obtained included individual peak positions and full width at half maximum (FWHM) of the contributing Gaussian ($W^G$) and Lorentzian ($W^L$) functions. The instrumental error correction was carried out using XRD peak widths of reference material LaB6 SRM660a and the following equations [14]:

$$(W_C^G)^2 = (W_M^G)^2 - (W_R^G)^2 \tag{2.6}$$

$$W_C^L = W_M^L - W_R^L \tag{2.7}$$

where the subscripts C, M and R refer to corrected, measured and reference peaks respectively. The corrected FWHM of the diffracted peak can then be calculated as [14]:

$$\Delta K = 0.5\{1.0692W_C^L + \sqrt{0.86639(W_C^L)^2 + 4(W_C^G)^2}\} \tag{2.8}$$

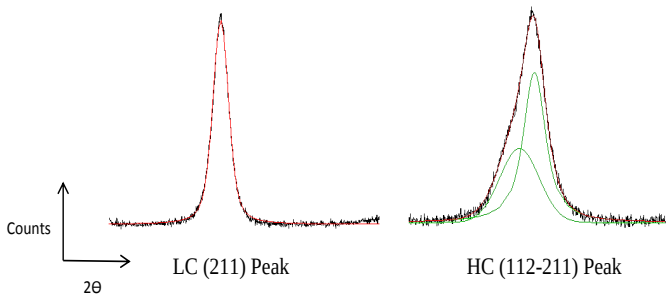


**Figure 2.8:** Example of peak splitting: 211 peak in LC steel splits up into 112-211 peak doublet in HC steel. Black lines are the original data, green lines are contributing peaks, red line is the resultant peak

#### Difficulties with HC steel

In case of HC steel, the BCT structure is more prominent due to higher carbon content. This can be seen in XRD graphs of HC in which every peak splits into two or three peaks which are very close to each other (see Figure 2.8). This happens because now the structure is not BCC with a single lattice parameter but BCT with two lattice parameters . The split peaks have different widths, but have very close $\theta$ or $K$ values. As a result, when these peak widths are used in plotting $\frac{(\Delta K-\alpha)^2}{K^2}$ *vs* $H^2$ or $\Delta K$ vs $K\overline{C}^{0.5}$ graphs, the data points for a combination of split peaks end up on top of each other and the result is a poor straight line fit and a lot of scattered data points (see Figure 2.9a and 2.10a). Such data will result in significant errors in calculation of dislocation density. One reason for this poor fit can be that the factor $H^2$ is defined for cubic materials here [35] and such factor for tetragonal structure has not been developed yet. Therefore modified Williamson-Hall method is well suited for cubic materials but a workaround method is needed if this method is to be used on tetragonal martensite.

To overcome this difficulty, first step is to make sure accurate peak positions of the split peaks are known. This is because when all the peaks are deconvoluted into contributing split peaks using Origin software, it was found that multiple split peak combinations can give same resultant peak. This can end up giving different peak positions for split peaks in a single HC sample. Therefore, advantage was taken of the fact that the ratio of intensities of a particular split peak-pair can be considered constant. For example, the intensity of (200) reflection in martensite is approximately twice to that of (002) reflection [36]. Such conditions were used as loose constraints while separating the peaks. This gave reasonably accurate peak positions in all samples. Now, instead of considering widths of individual split peaks, average of all split-peak pairs was calculated and plotted in the graph as width of corresponding original single peak. This gave good straight line fits and less data scatter as shown in Figure 2.9b and 2.10b.

### 2.5.2 Calculation of Carbon Concentration in Martensite Interstitials

Carbon concentration in interstitial sites is estimated by calculating the change in lattice parameters from XRD peak positions using Bragg's Law:

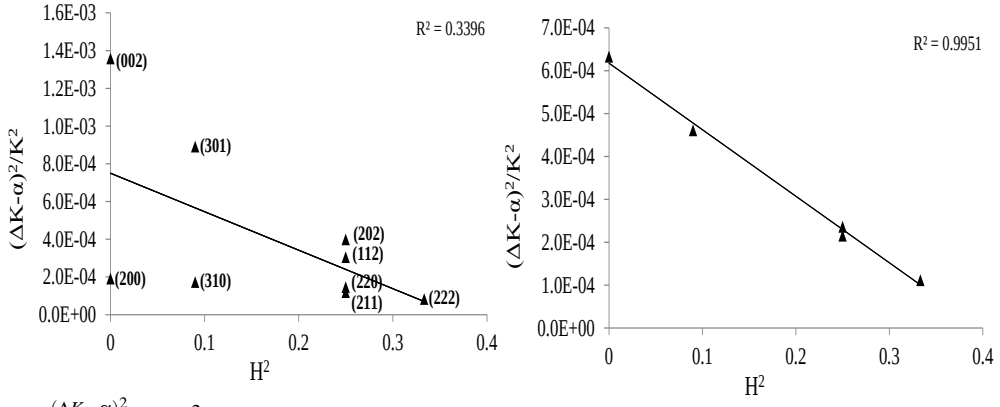


**(a)** $\frac{(\Delta K-\alpha)^2}{K^2}$ *vs* $H^2$ plot without width averaging **(b)** $\frac{(\Delta K-\alpha)^2}{K^2}$ *vs* $H^2$ plot after width averaging

**Figure 2.9:** $\frac{(\Delta K-\alpha)^2}{K^2}$ *vs* $H^2$ plots for a representative HC sample. In (b), peak width is obtained as the average FWHM of split peaks

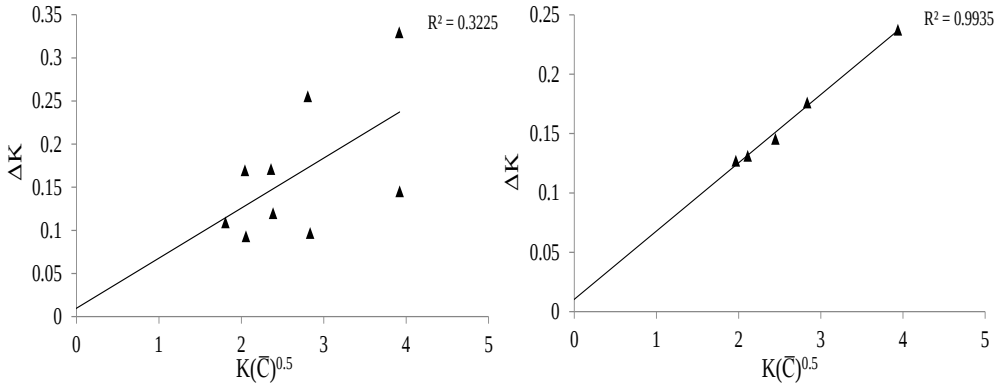


**(a)** $\Delta K$ vs $K\overline{C}^{0.5}$ plot without width averaging **(b)** $\Delta K$ vs $K\overline{C}^{0.5}$ plot after width averaging

**Figure 2.10:** $\Delta K$ vs $K\overline{C}^{0.5}$ plots for same HC sample used in Figure 2.9. In (b) peak width is obtained as the average FWHM of split peaks

$$\lambda = 2dsin\theta \tag{2.9}$$

and the following relation for cubic materials:

$$a = d\sqrt{h^2+k^2+l^2} \tag{2.10}$$

where $\lambda$ is the wavelength of the radiation used, $\theta$ is the angle of the diffracted beam, '$a$' is the lattice parameter,$d$ is interplanar distance and (hkl) are the miller indices of the reflecting plane. The values for '$a$' obtained from different peaks differ slightly from each other. This is because when equation 2.9 is plugged into equation 2.10, it is the error in sin $\theta$ and not error in $\theta$ that determines the error in '$a$'. Error in sin $\theta$ is lesser at high diffraction angles ($\theta = 90$ deg or $2\theta = 180$ deg). Unfortunately, peaks

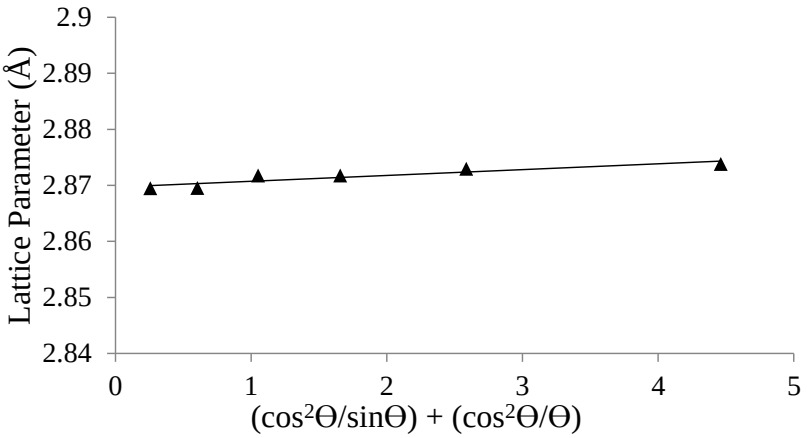


**Figure 2.11:** An example of lattice parameter vs nelson-riley function plot to estimate accurate lattice parameter for a representative LC sample

are not observed at this high angle. Therefore, values of '$a$' are plotted with a function of θ to get a straight line as [31]:

$$a = a_0 + m\left[\frac{cos^2\theta}{sin\theta} + \frac{cos^2\theta}{\theta}\right] \tag{2.11}$$

where $a_0$ is the correct lattice parameter, $m$ is the slope and $\left[\frac{cos^2\theta}{sin\theta} + \frac{cos^2\theta}{\theta}\right]$ is called the Nelson-Riley Function which goes to 0 at θ = 90 deg and thus the correct lattice parameter is obtained as $a = a_0$. An example of this plot is shown in Figure 2.11. The change in lattice parameter is given as:

$$\Delta a = a_0 - a_{Fe} \tag{2.12}$$

where $a_{Fe}$ is the lattice parameter of pure iron or a highly annealed steel sample of same composition ($a_{Fe}$ = 0.286575 nm in [13]). If it is assumed that the interstitial carbon content causes the change in lattice parameter, then this content can be calculated using the following approximate relationship obtained using independent calibration data [5]:

$$Weight\%\ carbon\ in\ martensite\ interstitials = 31\ \times\ \Delta a \tag{2.13}$$

In HC steel, peak splitting takes place as explained earlier. Therefore, each split peak gives two parameters $c$ and $a$. Average $c/a$ values are calculated by averaging c/a values from (002-200), (112-211) and (202-220) peak doublets [36]. This $c/a$ ratio can be used to find carbon in interstitial sites using following equation [37]:

$$c/a = 1 + 0.01X \tag{2.14}$$

where $X$ is the number of carbon atoms per 100 Fe atoms. $X$ is then converted to weight% carbon content.

### 2.5.3 Calculation of Retained Austenite Fraction and its Carbon Content

The retained austenite fraction is calculated from information about integrated intensities of XRD peaks in the sample. If there are two phases present in the sample, austenite ($\gamma$) and ferrite or martensite ($\alpha$), then austenite fraction is calculated as [38]:

$$f_r = \frac{\frac{1}{n_\gamma}\sum\frac{I^\gamma_{hkl}}{R^\gamma_{hkl}}}{\frac{1}{n_\alpha}\sum\frac{I^\alpha_{hkl}}{R^\alpha_{hkl}} + \frac{1}{n_\gamma}\sum\frac{I^\gamma_{hkl}}{R^\gamma_{hkl}}} \tag{2.15}$$

where (hkl) are the miller indices of the diffraction plane, $n_\gamma$ and $n_\alpha$ are the number of peaks of austenite and ferrite taken into consideration, $I$ is the integrated intensity of the observed peaks, and $R$ is the theoretical intensity of the peaks and is obtained from [39].

The carbon content in retained austenite is calculated using following equation which estimates the austenite lattice parameter as a function of composition:

$$a_\gamma = 3.556 + 0.0453x_c + 0.00095x_{Mn} + 0.0056x_{Al} \tag{2.16}$$

where $a_\gamma$ is observed lattice parameter in $\mathring{A}$ and $x_c$, $x_{Mn}$ *and* $x_{Al}$ are in weight% [40]. $a_\gamma$ is calculated by applying Bragg's Law (equation 2.9) and equation 2.10 for cubic materials on austenite peaks observed in XRD.

## 2.6 Hardness Measurements

After heat treatment in were polished using SiC abrasive sheets and at last using diamond paste of $1\mu$. Vickers 1 Kg hardness was measured using Struers Durascan tester over polished surface of the dilatometer samples. Hardness was measured at minimum of 10 points and the average value along with standard error reported in the results.

## 2.7 Cryogenic Treatment

A second set of samples was heat treated in dilatometer but was also given cryogenic treatment by placing the samples in liquid nitrogen for 15 seconds. Such samples are denoted by suffix '-N' in their name. So 'LC-N' and 'HC-N' stand for LC and HC alloys cooled in liquid nitrogen. The reason for cryogenic treatment, as will be discussed later, was to obtain fully martensitic microstructure with minimum amount of retained austenite.

# Chapter 3

# Results

## 3.1 Design of Heat Treatments

Pure Iron exists as $\gamma$ phase above 912°C as can be seen in figure 1.1. With addition of more and more carbon as alloying element, this minimum temperature decreases. The austenitizing temperature to be employed should be well above this temperature with sufficient holding time in order to ensure complete conversion of material into austenite and homogeneous distribution of alloying elements in the material. Once transformed, austenitizing temperature and time affects the prior austenite grain growth. The aim here was to obtain martensite with different PAGS for both type of alloys.

### 3.1.1 Dilatometry

Before actual heat treatments, it is important to carefully chose the process parameters. In alloy with same composition as LC, complete austenitization occurs by holding at 900°C for 3 minutes [14]. Subsequently, cooling at the rate of 20°C $s^{-1}$ or above gives fully martensitic structure [13, 14]. In preliminary experiments, it was observed that an increase in temperature has a larger effect on PAGS than an increase in holding time. Moreover, with increasing austenitizing time, a more heterogeneous PAGS distribution with evidence of abnormal grain growth was observed.

Considering above points, only austenitization temperature was varied to obtain different PAGS. Five different austenitizing temperatures were chosen :900, 950, 1000, 1100 & 1200°C. Heating and cooling rate were fixed at 5°C $s^{-1}$ and 20°C $s^{-1}$ respectively. Austenitizing time was kept constant at 5 minutes. All dilatometry heat treatments carried out on LC and HC alloy samples are shown in figure 3.1.

The change in length vs temperature plots for all specimens heat treated in dilatometer are shown in figures 3.2a and 3.3a. From the start of the experiment, till about 450°C, the curves are a straight line indicating linear thermal expansion of constituting austenite (FCC) and martensite (BCT) phases. There is a sudden contraction in length, seen as a bump at about 500°C. The curves are again straight line till they reach $Ac_1$ temperature. From $Ac_1$ to $Ac_3$ temperature, transformation into austenite phase takes place accompanied by decrease in length, since austenite has lower spe-

cific volume than martensite.The theoretical $Ac_1$ and $Ac_3$ temperature for Fe-C-Mn-Si alloy system can be calculated using following composition based equations [41]:

$$Ac_1 = 742 - 29(C) - 14(Mn) + 13(Si) \tag{3.1}$$

and

$$Ac_3 = 925 - 219\sqrt{C} - 7(Mn) + 39(Si) \tag{3.2}$$

where $Ac_1$ and $Ac_3$ are in °C and concentration of alloying elements is in weight %. Using above equations, $Ac_1$ and $Ac_3$ for LC alloy are approximately 720 °C and 840 °C and for HC alloy their value is 696 °C and 793 °C. These values are not very accurate, but at least they show that $Ac_3$ is more sensitive to carbon content than $Ac_1$. In figures 3.2a and 3.3a also, it can be seen that difference in $Ac_3$ temperature of both alloys is higher than difference in $Ac_1$ temperature. From $Ac_3$ till the end of heating process, linear expansion of austenite phase takes place.

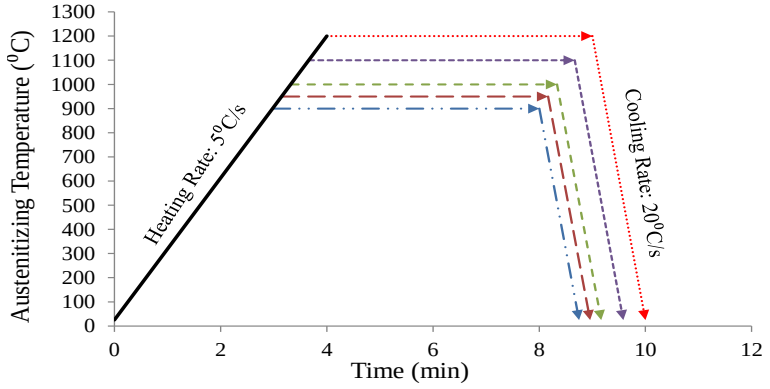


**Figure 3.1:** Dilatometry heat treatments on LC and HC alloy samples

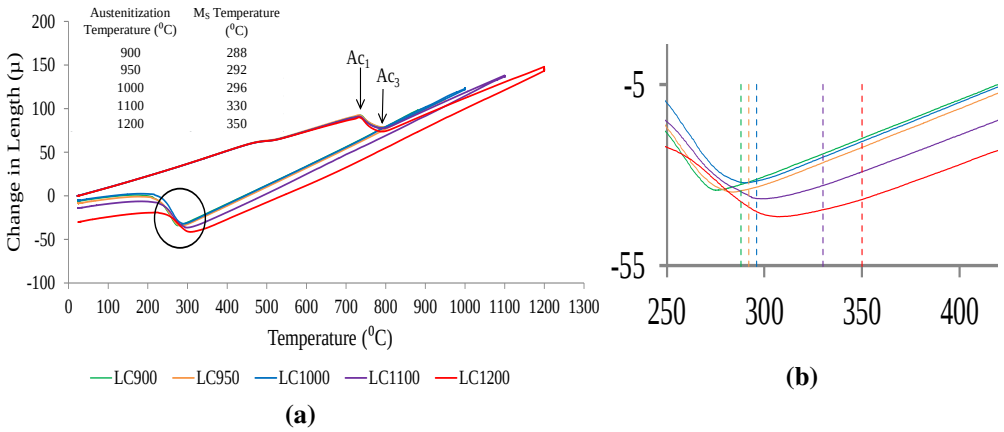


**Figure 3.2:** (a) Change in length vs temperature plot for LC samples heat treated in dilatometer (b) Magnified image of encircled area indicating $M_S$ temperatures by colored vertical lines

During cooling, no remarkable feature is observed until the samples reach the martensite start ($M_S$) temperature. Below this temperature, there is a length expansion, signifying the formation of martensite. The $M_S$ temperature increases for high austenitization temperatures, as can be seen from tables in figures 3.2a and 3.3a. Figures 3.2b and 3.3b show the $M_S$ temperatures for different LC and HC samples with corresponding colored vertical lines, calculated using offset method as described in [42]. An offset strain of 0.02% was used here. However, the $M_S$ temperatures are difficult to distinguish from the figures because the curves overlap.

At the end of cooling, it can be seen that the curves do not become straight enough to signify completion of martensitic transformation and linear contraction of martensite phase. This means that some austenite is retained at room temperature. In order to obtain maximum martensite fraction possible, another set of alloy samples were heat treated similarly but were further given cryogenic treatment in liquid nitrogen (-196°C) for 15 seconds before bringing them back to room temperature, and were designated as LC-N and HC-N.

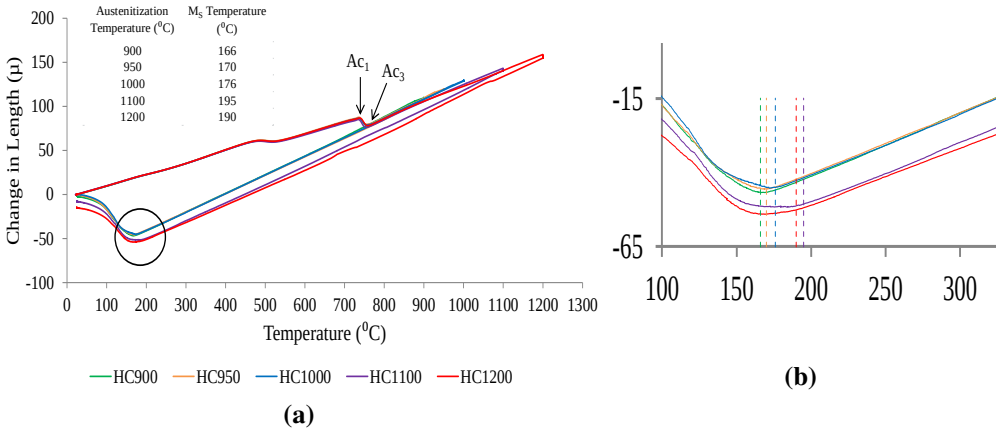


**Figure 3.3:** (a) Change in length vs temperature plot for HC samples heat treated in dilatometer (b) Magnified image of encircled area indicating $M_S$ temperatures by colored vertical lines

### 3.1.2 Prior Austenite Grain Size (PAGS) Statistics

Figure 3.4 shows the distributions of PAGS obtained after heat treatments in the form of box and whisker plots. The whiskers denote the minimum and maximum values, while the box represents 25th, 50th (median) and 75th percentile values in the distribution and point labels inside the box denote average PAGS values. Both LC and HC alloy types show similar distributions. In figure 3.5, it can be seen that although the scatter in grain size increases with austenitizing temperature, the average grain size at any austenitizing temperature remains almost the same in both alloys. The difference in carbon content of alloys does not significantly affect the PAGS.

## 3.2 Microstructure Characterization

### 3.2.1 EBSD and SEM

The aim of EBSD measurements was to know the magnitude of variation of martensite block size with PAGS, and of SEM was to check for the presence of carbide precipitates. Due to a limitation of time and resources, only three PAGS samples of LC-N and HC-N were studied. Figures 3.6 and 3.7 show the inverse pole color maps (left) and SEM images (right) for the samples austenitized at 1000°C, 1100°C and 1200°C. The coloured blocks in EBSD figures represent different crystallographic orientations. In LC-N samples, these blocks exhibit elongated structures. Their length increases with increasing PAGS, and is delimited by packet size. In HC-N samples this trend is followed too, but there are many less-elongated or uniformly shaped blocks present. As a result, aspect ratio (height/width) of martensite blocks appears less in case of HC-N alloy than in LC-N alloy. The length of the blocks in HC-N samples is significantly reduced due to which their microstructure also appears more distorted in SEM images.

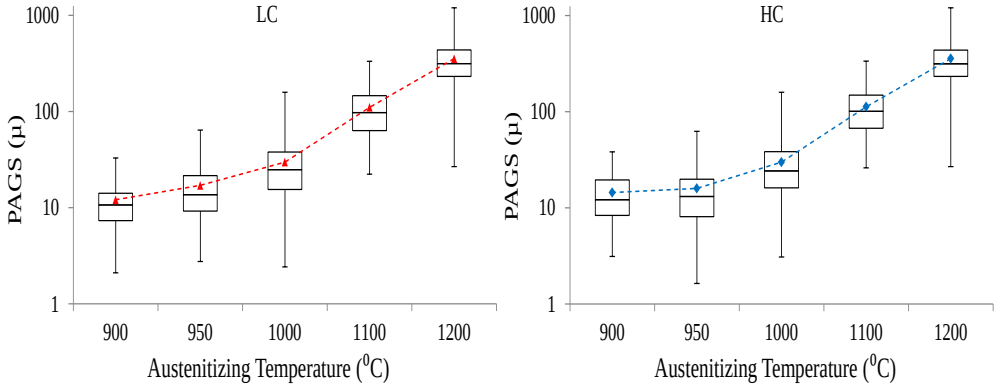


**(a)** PAGS distribution in LC **(b)** PAGS distribution in HC

**Figure 3.4:** PAGS distribution in the form of box and whisker plot

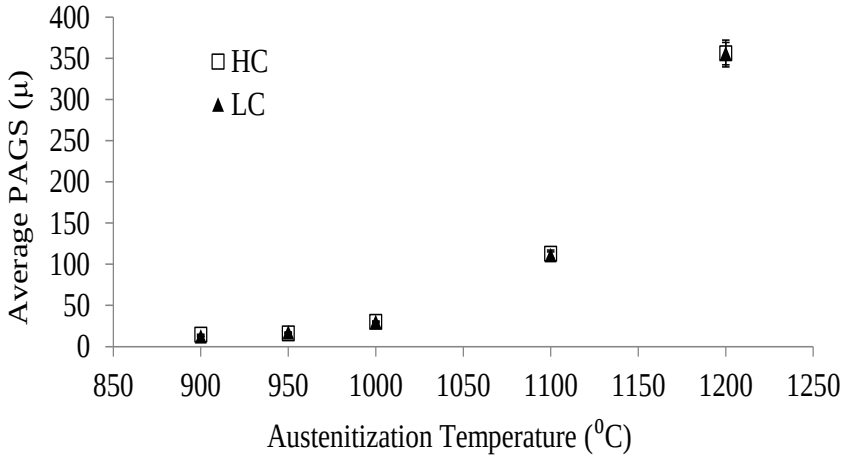


**Figure 3.5:** Variation of average PAGS size with austenitizing temperature in LC and HC alloys. Error bars denote the experimental standard error, but are too small to be distinguished

### Variation of Block Width

Block widths were calculated using EBSD misorientation profiles as described previously in section 2.4.1. The variation of block widths with PAGS in both LC-N and HC-N alloys are shown in figure 3.8. Although there is a decrease in average widths of the blocks in going from LC-N to HC-N alloy, very weak increase in the widths is observed with increasing PAGS.

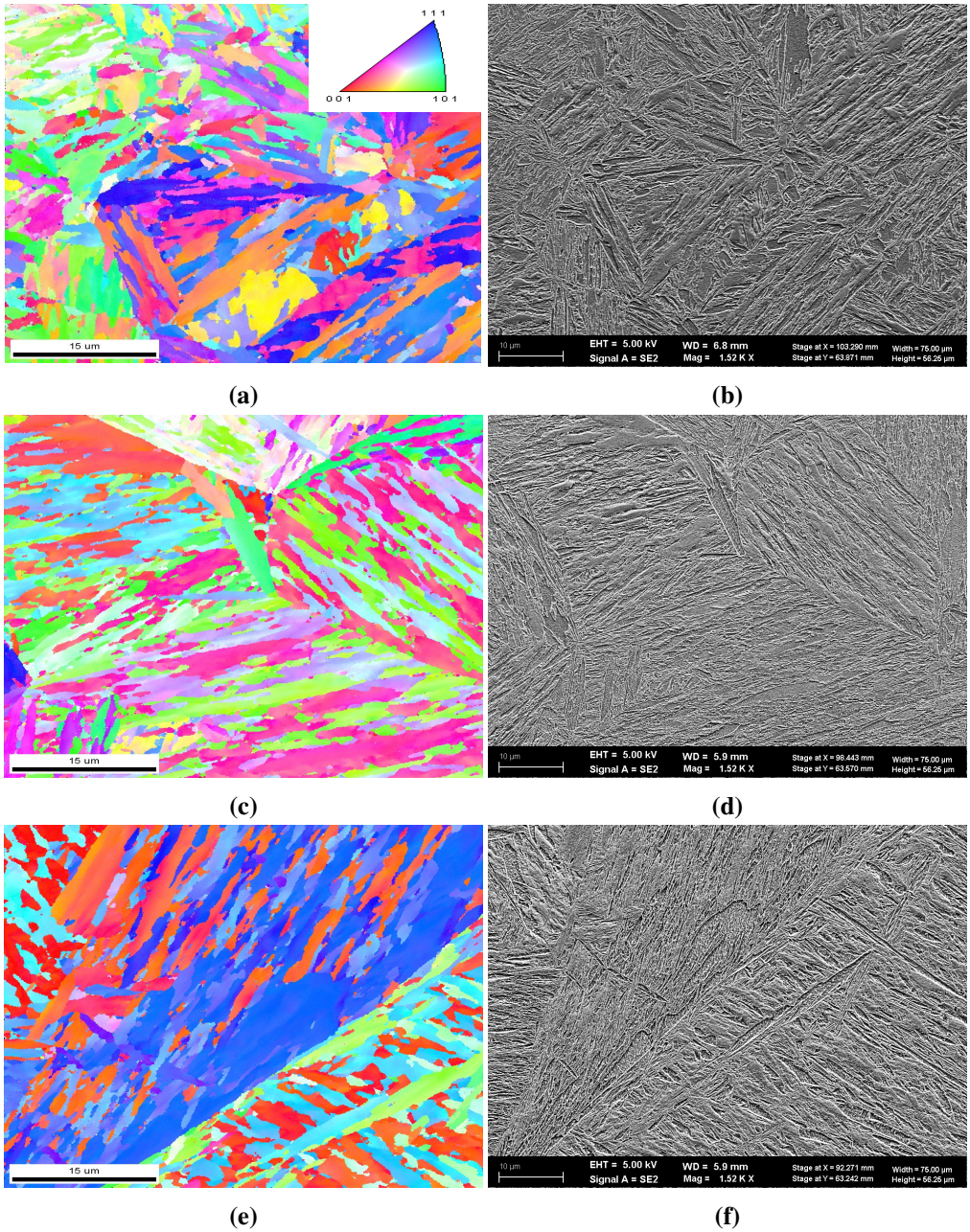


**Figure 3.6:** EBSD (left) and SEM (right) images of LC-N martensitic microstructures obtained after austenitization at 1000°C (a, b); 1100°C (c, d); 1200°C (e, f). The color legend for all images is shown in (a)

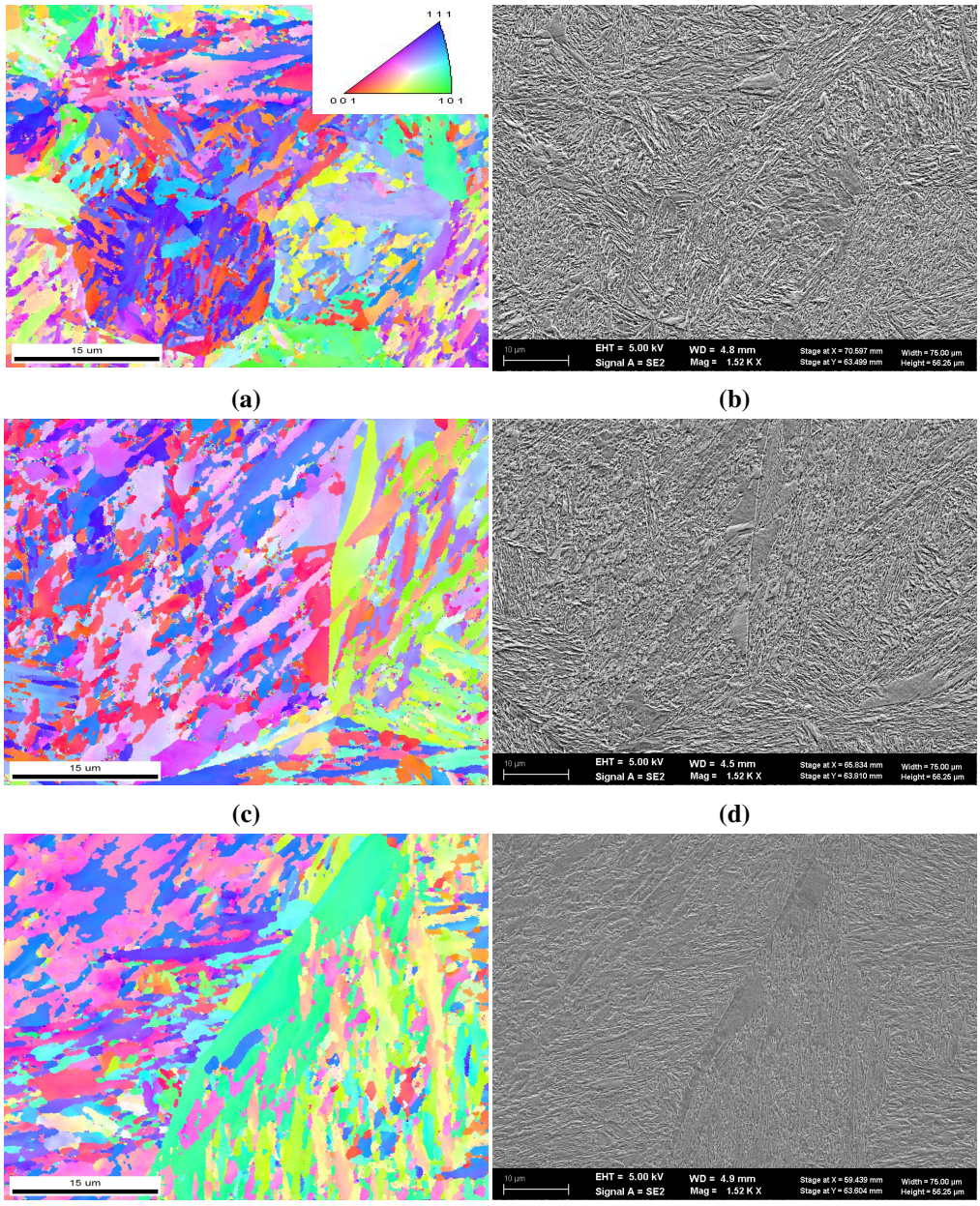


**Figure 3.7:** EBSD and SEM images of HC-N martensitic microstructures obtained after austenitization at 1000°C (a, b); 1100°C (c, d); 1200°C (e, f).The color legend for all images is shown in (a)

### Carbides Formation

It was difficult to identify carbide particles from the available SEM images. Only in LC-N sample with highest grain size, some needle-shaped carbides can be identified, as shown in figure 3.9.

### 3.2.2 XRD Measurements

Representative XRD diffractograms of LC and HC samples are shown in figures 3.10a and 3.10b. Peaks indicated by blue color and red color are austenite and martensite peaks respectively. (h,k,l) indices of diffracting planes are shown on top of corresponding peaks. Austenite peaks are present in HC alloy but not in LC alloy. Also, martensite peaks in HC alloy are broader than in LC alloy, and are actually combination of two or more peaks. The diffractograms for LC-N and HC-N samples are similar to those of LC and HC samples, and hence are not shown.

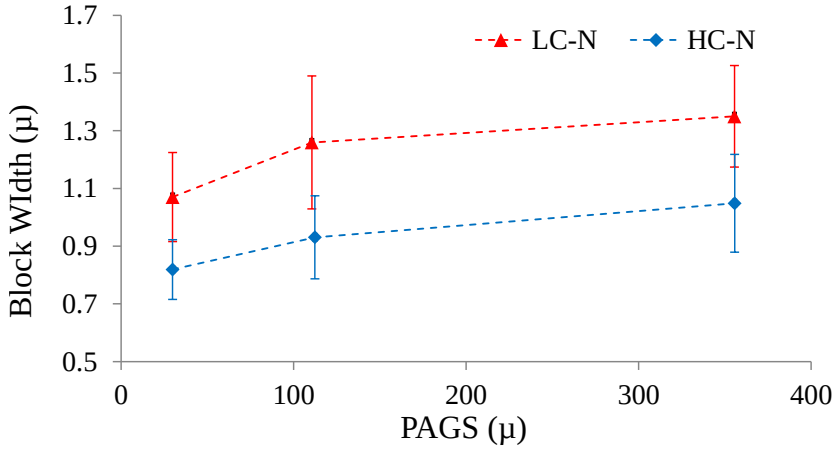


**Figure 3.8:** Variation of block width with PAGS

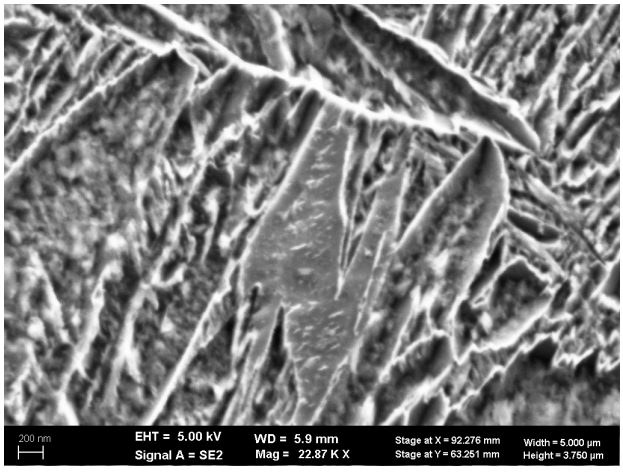


**Figure 3.9:** Needle-shaped carbides in LC1200 sample

#### Dislocation Density

The variation of dislocation densities in martensite vs PAGS, as calculated using modified Williamson - Hall method, is shown in figure 3.11. In LC alloy (figure 3.11a), initially the decrease in dislocation density is steep and becomes gradual at higher PAGS. In HC alloy (figure 3.11b), a sharp decrease in dislocation densities is evident initially, but thereafter it is difficult to identify any trend. After cryogenic treatment,

dislocation densities in two smallest and the largest PAG is not affected much but it seems to increase significantly in mid-size PAGs, both in LC-N (figure 3.11c) and HC-N (figure 3.11d) samples.

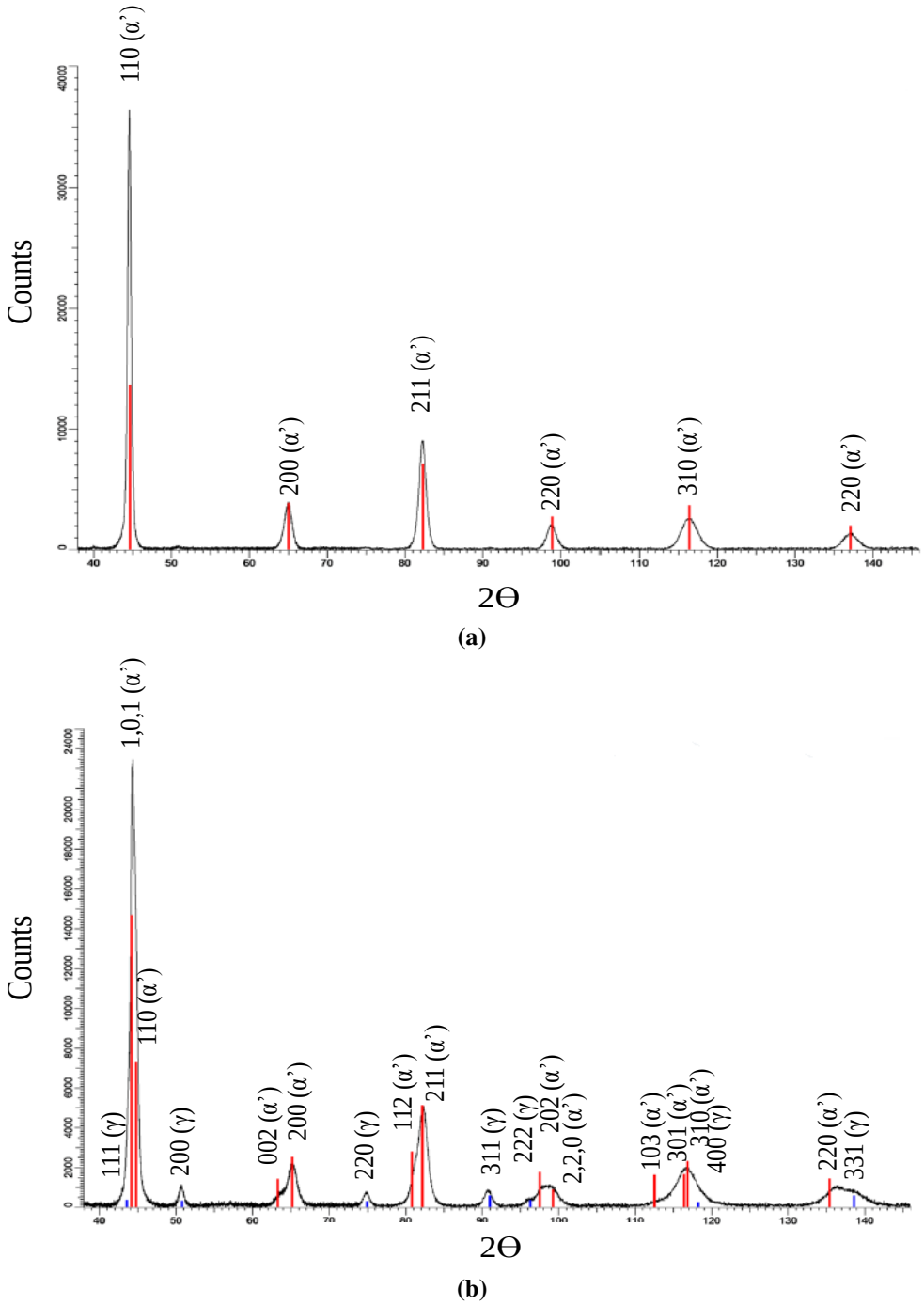


**Figure 3.10:** XRD diffractograms for a representative (a) LC (b) HC alloy sample. (hkl) indices of diffracted plane and phase are mentioned alongside corresponding peaks

### Carbon Concentration in Martensite Interstitials

Variation in weight% carbon in martensite interstitials with PAGS for all samples is shown in figure 3.12. An increase in interstitial carbon with PAGS can be identified in LC alloy (figure 3.12a), but in HC alloy there is no such trend (figure 3.12b). After cryogenic treatment, there is an increase in carbon concentration in interstitials, which was not expected. This increase is more for martensite with mid-size PAGs while for small and large PAGs, change is insignificant.

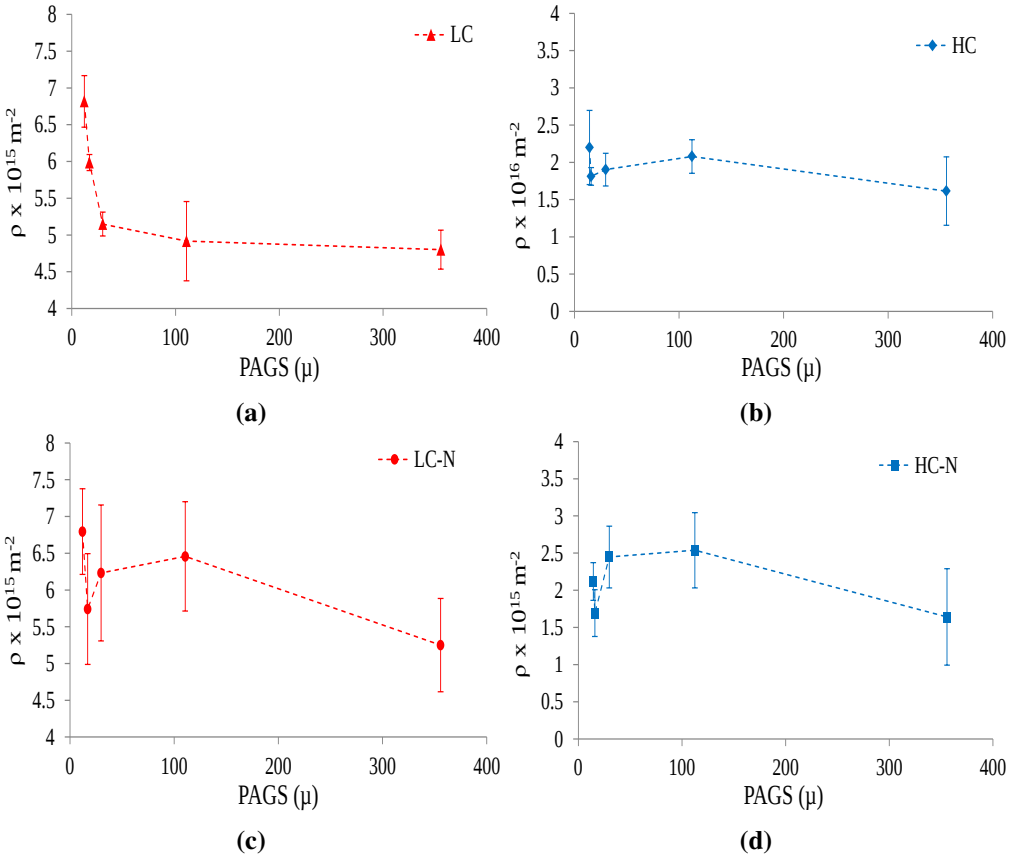


**Figure 3.11:** Variation of dislocation density with PAGS in (a)LC (b)HC (c)LC-N and (d)HC-N samples

### Retained Austenite Fraction and its Carbon Content

Variation of volume fraction retained austenite with PAGS in HC and HC-N samples is shown in figure 3.13a. No significant dependence of retained austenite volume fraction on PAGS is observed in either HC or HC-N samples. A surprising observation is that even after cryogenic treatment, the volume fraction retained austenite in HC-N samples is still high. No such calculations were performed for LC or LC-N samples, since in those cases austenite peaks in XRD measurements were negligible.

Due to partitioning of carbon into austenite during martensitic transformation [43], the retained austenite may have higher carbon concentration than the average carbon

concentration in the alloy. To measure this, retained austenite lattice parameters were calculated using the Nelson-Riley method, described previously in chapter 2. The carbon concentration at interstitial sites is calculated and its variation with PAGS is shown in figure 3.13b. It was found that carbon concentration in austenite has a uniform value which is independent of PAGS.

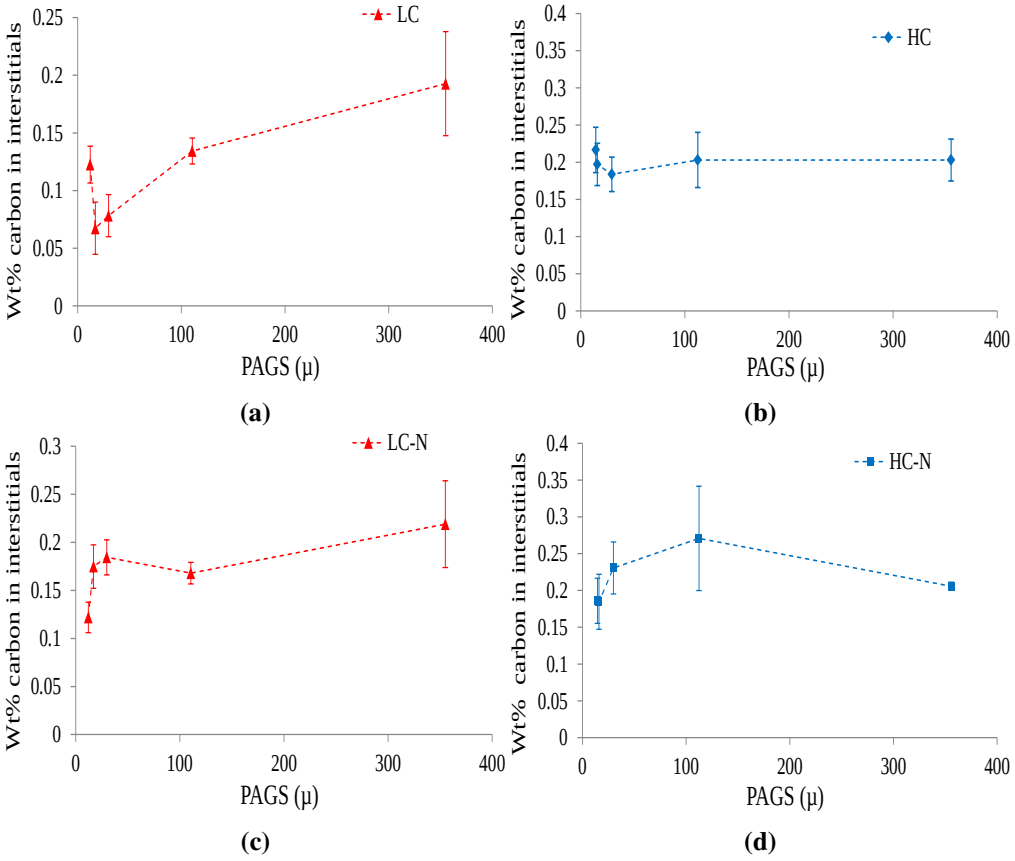


**Figure 3.12:** Weight% Carbon in Martensite Interstitials vs PAGS in (a) LC (b) HC (c) LC-N and (d) HC-N samples

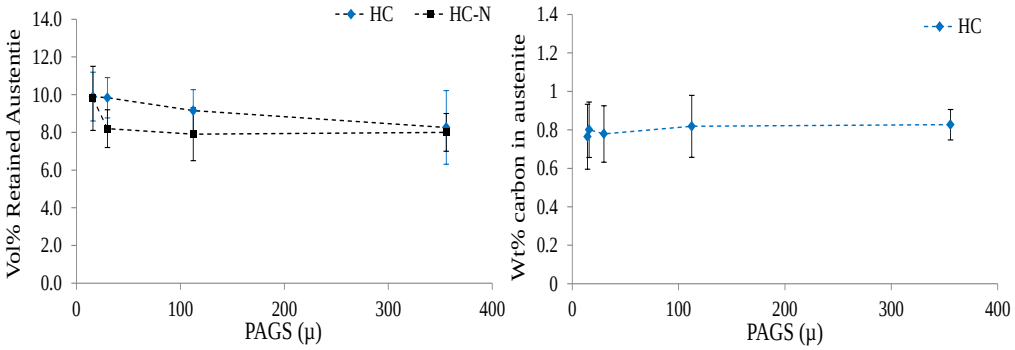


**(a)** Volume% retained austenite vs PAGS **(b)** Weight% C in retained austenite vs PAGS

**Figure 3.13:** Variation of (a) volume% retained austenite and (b) weight% C in retained austenite vs PAGS

## 3.3 Hardness Measurements

Figure 3.14 shows the variation of average HV1 hardness values with the average PAGS in all samples. There is an increase in hardness with increase in carbon content from LC to HC and LC-N to HC-N alloy. Hardness in HC and HC-N samples does not show significant variation with PAGS. Hardness of LC and LC-N martensite varies with PAGS but any definite trend is absent.

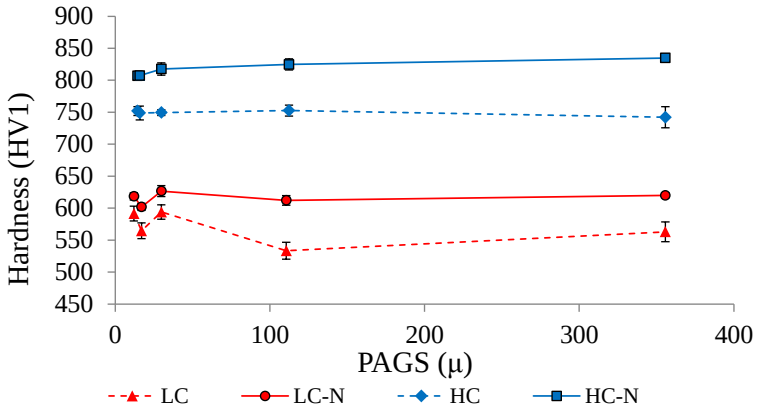


**Figure 3.14:** Variation of average hardness with average PAGS in LC, LC-N and HC, HC-N samples

# Chapter 4

# Discussion

## 4.1 Effect of Carbon content and PAGS on Transformation Kinetics

Several conclusions can be drawn from the dilatometer curves of LC and HC alloys. The decrease in length at about 500°C while heating is due to precipitation of carbides, and is more in HC than in LC. This is expected since HC has higher carbon content. The decrease in length during transformation of material into austenite (from fcc to bcc, between $Ac_1$ and $Ac_3$) is less in HC than in LC. This may be attributed to the fact that HC may have contained relatively higher amount of retained austenite than LC. LC may be having more martensite, due to which there is larger contraction in length in LC. It is also seen that $M_S$ temperatures are lower in HC alloy which has higher total carbon content. Carbon is an element which stabilizes austenite [44]. The higher the carbon content, the higher the undercooling required to trigger martensitic transformation. Several models developed in the past show that $M_S$ temperature decreases with increasing carbon content [45, 46, 47]. According to [47], $M_S$ is given by:

$$M_S = 475.9 - 335.1x_C - 34.5x_{Mn} - 1.3x_{Si} - 15.5x_{Ni} - 13.1x_{Cr} - 10.7x_{Mo} - 9.6x_{Cu} + 11.67\ ln(d_\gamma) \quad (4.1)$$

where the amount of each alloy element ($x_i$), average PAGS ($d_\gamma$), and $M_S$ temperature are expressed in terms of weight %, $\mu$, and °C respectively. Equation 4.1 gives only very rough estimate of $M_S$ as can be seen by comparing the experimental values to those predicted by the equation in figure 4.1.

The $M_S$ temperature also increases slightly with austenitization temperature or PAGS. A possible explanation is that at lower grain size, prior austenite is strengthened due to Hall-Petch effect and increased dislocation density [45, 48, 22]. Therefore, a lower PAG will offer more resistant to plastic deformation required for formation of martensite [45, 48]. In HC, the prior austenite is strengthened even more due to more carbon content. This may be the reason why considerable austenite fraction is still

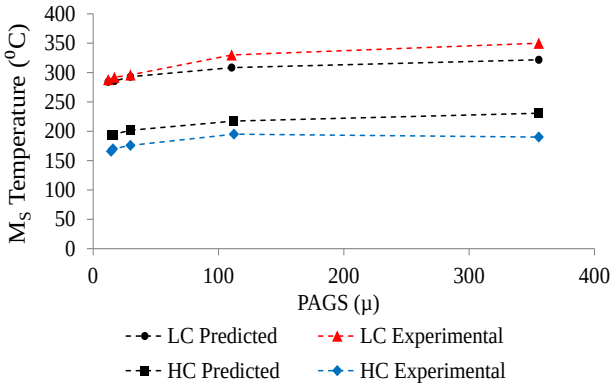


**Figure 4.1:** Comparison of experimentally obtained values and predicted values of $M_S$ temperatures from equation 4.1

found in HC, even after cryogenic cooling. The curves also become less sharp near $M_S$ temperatures with increasing PAGS, a phenomena referred to as 'low start'. Slow start is expected if a dispersion of $M_S$, rather than a single value, exists in the specimen [49]. Chemical inhomogeneity may be a reason for it, but in present case most probable reason is the increased scatter in PAGS values with increasing austenitization temperature as inferred from figure 3.4.

Another interesting observation is that although similar increase in PAGS takes place both in LC and HC alloys, the $M_S$ in LC increases more than in HC with increasing austenitizing temperature. Such a phenomena was also observed in [45]. The reason is still unclear, but it shows that austenite strengthening is more sensitive to PAGS if the carbon content is lower.

In [48], the authors attribute the decrease in $M_S$ temperature with decreasing PAGS to prior austenite strengthening as well as decreasing aspect ratio (height/width) of laths. Therefore, it is possible that the aspect ratio of laths in LC decreases rapidly with decreasing PAGS, while in HC it does not, explaining little change in $M_S$ in HC. However, these are just speculations and proper study in this regard needs to be carried out.

## 4.2 Effect of Carbon content and PAGS on Block Size and Carbide Precipitation

The martensite blocks become shorter in length and finer in width when total carbon content increases. This can be seen in figure 3.8 and by comparing figures 3.6 and 3.7. In [50] also, authors observed decrease in martensite block and packet size with increasing carbon content. A possible reason, as suggested in [50], is that the strain of martensitic transformation is not easily relieved by self accommodation in austenite matrix if the carbon content is higher, due to greater solid solution hardening of austenite by carbon. Therefore, self accommodation by martensite should take place. For self accommodation, it is necessary that block and packet size decrease.

In steels with high $M_S$ temperature, carbon mobility is sufficient to cause precipitation of carbides during quenching from $M_S$ to room temperature. This process is called autotempering [4]. The higher the $M_S$, more the autotempering [51]. HC has low $M_S$, so significantly lower amount of carbides is expected in HC than in LC alloys. Some needle-shaped carbides were observed only in LC-N sample with largest PAGS (see figure 3.9) and no carbides were found in HC-N samples. Perhaps the carbide particles are very small and difficult to detect.

The size and morphology of carbides depends upon the $M_S$ temperature. Coarser carbides having an elongated shape are formed if $M_S$ temperature is higher, while if the $M_S$ temperature is low, globular shaped fine carbides are formed [13, 52]. Despite this, we cannot conclude anything about the variation of carbide volume fraction with $M_S$ temperature (or PAGS). This is because even though the size of carbide particles increases at higher $M_S$, their number may decrease since now the dislocation density is less and therefore there are less number of sites for carbon atoms to segregate to and form carbides [13]. Therefore, in present study, it is assumed that volume fraction of carbides remains practically constant with PAGS. After this assumption, it can not be a cause for variation of any other quantity with PAGS and hence has been neglected in further calculations. At the end of next section, possible repercussions this assumption might have on the conclusions will be discussed.

## 4.3 Relation between Carbon content, PAGS and Dislocation Density

In chapter 1, it was discussed that there is some controversy regarding how the distribution of total carbon content to martensite interstitial sites and to vicinity of dislocations, is linked with martensite dislocation density and PAGS variations. When the total carbon content is increased, dislocation density increases but interstitial carbon content does not increase much. And when PAGS is varied, dislocation density and interstitial carbon content both vary but it is still not clear how. In [29], the authors develop a microstructural evolution model (given by equation 1.10), explaining the relation between dislocation density, lath size and total carbon content, thus linking these three features. The authors assume that no carbon is left in true interstitial sites. Also, the model does not bring into the picture the role of PAGS, which is an important factor as evident from the controversies.

In case of LC alloy, a decrease in dislocation density and an increase in interstitial carbon content with increasing PAGS is evident, as shown in figure 4.2. However, no such remarks can be made about HC alloy. It appears as if in HC these quantities do not vary significantly with PAGS.

It was observed that theoretically, is it possible to obtain trends which agree with the experimentally obtained trends of figure 4.2, by making slight modification in equation equation 1.12 as follows. Suppose the fraction of carbon atoms available in martensite for segregation to dislocations is given by:

$$x_c^{\alpha'} = x_{c,tot}^{\alpha'} - x_{c,ppt}^{\alpha'} - x_{c,intsl}^{\alpha'} \tag{4.2}$$

where $x_{c,intsl}^{\alpha'}$ term is for carbon content still present in true martensite interstitial sites. Lath width, $d_{lath}$ depends only on total carbon content [29]. Then, according to equation 1.13, $\rho \propto (x_c^{\alpha'})^{\frac{2}{3}}$. Now, $x_{c,ppt}^{\alpha'}$ = constant or zero (according to assumption regarding precipitates mentioned in section 4.2). So, for LC, an increase in $x_{c,intsl}^{\alpha'}$ values with increasing PAGS as observed in figure 4.2b, explains the corresponding decrease observed in martensite dislocation densities with increasing PAGS . In HC samples, $x_{c,intsl}^{\alpha'}$ is nearly constant with PAGS as shown in figure 4.2b. This means that for HC samples, $x_c^{\alpha'}$ and thus ρ values should not show any trend with PAGS. This is what is observed experimentally as shown in figure 4.2a.

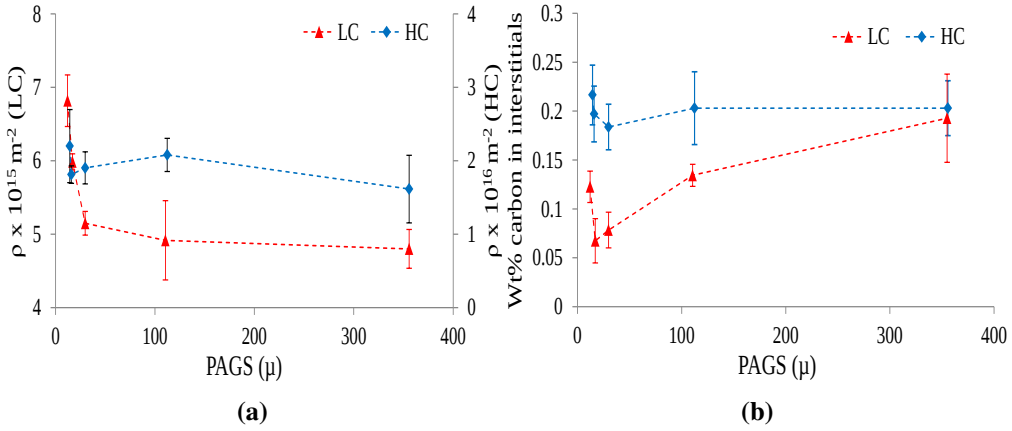


**Figure 4.2:** Comparison of (a) Martensite dislocation densities and (b) Carbon concentration in martensite interstitials in LC and HC alloy samples

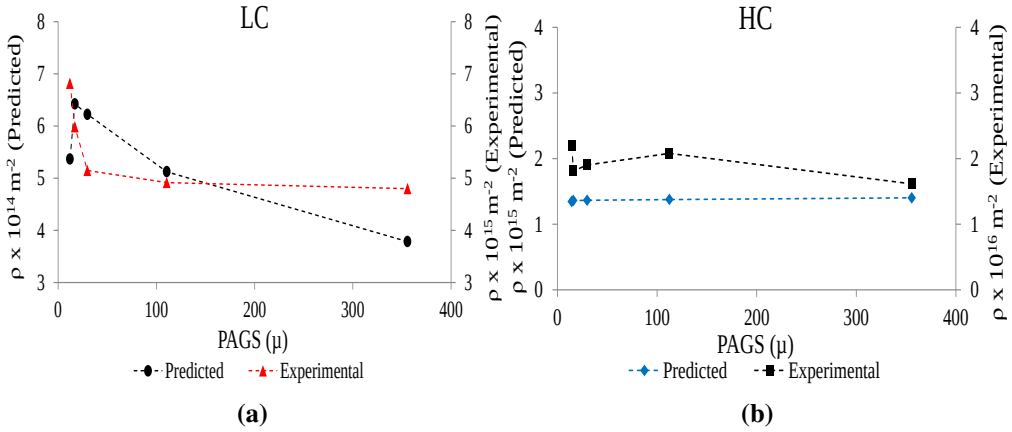


**Figure 4.3:** Comparison of dislocation densities obtained from experiments and predicted using model equations 1.13 & 4.2. Note that they differ by an order of magnitude

The dislocation density values obtained from experiment and the model represented by

equation 1.13 and 4.2 are compared in figure 4.3. Although the model underestimates the dislocation densities by an order of magnitude, it is worth noting that by slightly modifying equation 1.12 into equation 4.2, we can produce trends which are in good agreement with experimentally obtained trends. In this way, the interdependence between dislocation density, carbon content and PAGS can be explained to some extent. Martensite dislocation density decreases with increasing PAGS [13, 24] due to which lesser carbon atoms segregate to dislocation. This causes an increase in interstitial carbon content with increasing PAGS in martensite [21]. Also, when total carbon content increases at fixed PAGS, major increase takes place in carbon atoms segregated at dislocations, and carbon content at interstitial sites does not increase much. However, this effect is more prominent at larger PAGS, as shown in figure 4.2b and also observed in [20].

Some comments can be made on validity of assumption regarding carbide precipitates. It was assumed that the volume fraction of carbides in martensite does not change with PAGS. In reality, larger PAGS results in higher $M_S$, due to which carbides become coarser [13, 52]. If we take this to be the evidence of increasing carbide volume fraction with increasing PAGS and incorporate it in equation 4.2, the theoretically obtained trend will become even more steep and will be more in agreement with the actual experimental trend in LC samples. Also, in case of HC alloy, even without considering carbon content in precipitates we are able to reproduce the experimentally obtained trend. This points to the fact that our initial assumption may very well be a reasonable one.

## 4.4 Effect of PAGS on Hardness

In figure 4.4, the strengthening contributions from dislocations, carbon in interstitials and block boundaries along with hardness values are plotted against PAGS for LC and HC steel alloys. Hardness can be expressed as a linear function of martensite strength, as in equation 1.9. Substitutional solid solution strengthening and precipitate strengthening remain constant with PAGS, and do not contribute much to variation in strength with PAGS. They are thus not shown in figure 4.4.

Contributions from strengthening mechanisms are calculated using respective equations as explained in section 1.3. The dislocation density is calculated using Taylor's equation: $\sigma_\rho = \alpha MGb\sqrt{\rho}$, where the values of different parameters used are $\alpha = 0.25$, M = 3, G = 80 Mpa, b = 0.284 nm for pure iron, obtained from [14]. Strengthening due to interstitial carbon is calculated from $\sigma_c = 1171.3X_C^{1/3}$, where $X_C$ is taken to be weight% carbon in martensite interstitials. Grain boundary strengthening is calculated using Hall-Petch relation: $\sigma_{gb} = k_{HP}/\sqrt{d_{block}}$. Value of $k_{HP}$ used is 0.21 MPam$^{\frac{1}{2}}$ for martensite block boundaries [53].

It is important to mention here that block size measurement was only performed for 3 PAGS samples of each LC-N and HC-N alloy types. It is assumed that the average block width after cryogenic treatment should not be different than that of before. Therefore, block width for LC and HC samples are taken to be same as LC-N and HC-N samples respectively. Also, approximate block widths for other two PAGS are

obtained by extrapolation.

In figure 4.4, it can be seen that the highest contribution to strength is by dislocations, followed by interstitial carbon strengthening. Several authors have also identified block size as an important contributor to martensite strength [16, 53, 54]. However, it contributes least to the overall strength here when compared to other strengthening mechanisms. Moreover, block size increases slightly with PAGS (figure 3.8) and therefore contributes less to overall variation of strength with PAGS. For LC alloy, hardness shows erratic variations because of opposing trends of dislocation and interstitial carbon strengthening. In HC alloy, interstitial carbon content and dislocation densities have similar values for all PAGS, as a result hardness too does not show much variation with PAGS.

Only the strengthening contribution from interstitial carbon atoms increase with increasing PAGS in LC, rest others follow a decreasing trend, even the precipitate strengthening and strengthening by segregated carbon atoms, which we haven't considered here, would decrease. Although it appears so, it is very far-fetched to say that interstitial carbon strengthening is able to counter contributions from all other strengthening mechanisms and give hardness an unchanging or increasing trend with increasing PAGS, as shown in some cases when we discussed the controversies in section 1.4. On the other hand, in HC, there is no appreciable change in dislocation density with PAGS. And hence, no appreciable change in other strength contributions as well. We have seen in the previous section that dislocation density is the main controlling factor behind other strengthening mechanisms. Prior austenite dislocation density controls the strengthening of austenite matrix and the $M_S$ temperature, while the martensite dislocation density controls the amount of carbon segregating to dislocations, carbon in the interstitial sites and also the characteristics of carbide precipitates. If these two controlling factors, under any circumstances, do not show much change with PAGS, then hardness will also not show any variation. These circumstances are most probably related to overall composition of the alloys, especially the carbon content.

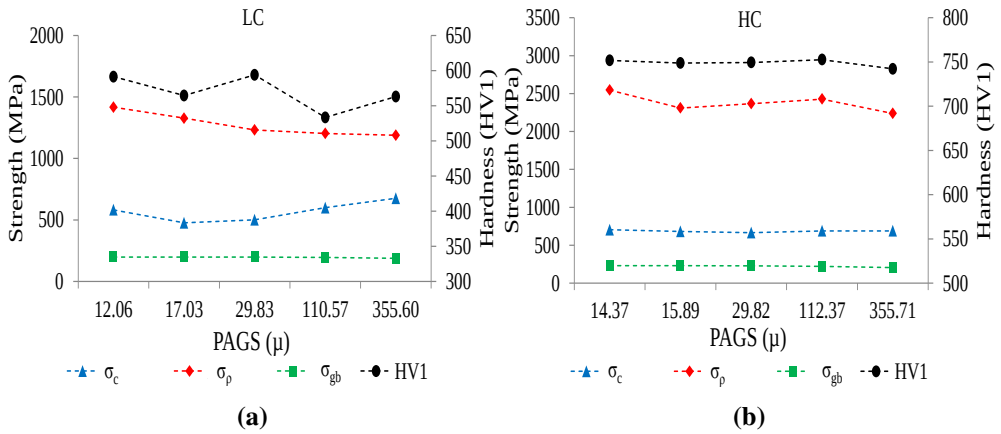


**Figure 4.4:** Strengthening contributions ($\sigma_C$, $\sigma_\rho$ & $\sigma_{gb}$) and Hardness vs PAGS in (a) LC alloy (b) HC alloy.

## 4.5 Effect of Cryogenic Treatment

For HC and HC-N samples, as shown in figures 4.5b and 4.5d, there is a general increase in dislocation density and carbon concentration in martensite interstitials (tetragonality) after cryogenic treatment and this increase is prominent in mid-size PAGs. This increase corresponds to decrease in volume fraction of retained austenite in same mid-size PAGs as shown in figure 3.13a. The carbon content in retained austenite before cryogenic treatment is higher than the surrounding martensite as shown in figure 3.13b. Therefore, new martensite formed at cryogenic temperature has greater tetragonality. This also raises the overall average tetragonality of the martensite. Newly formed martensite has higher dislocation density as well because it is formed from more stable austenite.

An unexpected result is that such an increase in interstitial carbon content and dislocation density is also observed in LC-N samples even though the volume fraction of austenite in both LC and LC-N samples is negligible (see figures 4.5a and 4.5c). There can be two reasons for this: First, it may be the case that fraction retained austenite in LC samples is low, and in LC-N samples it is even lower, but the austenite peaks in XRD diffractograms of these samples are very small and indiscernible.

Second explanation can be given on the basis of residual stresses in martensite. Previous studies have proved that after cryogenic cooling and tempering, larger relaxation of residual stresses takes place compared to conventionally quenched and tempered steels [55, 56, 57]. The degree of supersaturation in martensite increases with decreasing temperature. This increases the lattice distortion and thermodynamic instability of the martensite. Carbon atoms are driven out to segregate to nearby defects to form clusters. These clusters may grow into nuclei for the formation of fine carbides on tempering [56]. Due to this, there is large relaxation of residual stresses in the lattice when the specimen is brought back to room temperature and tempered, more than the conventional cooling and tempering process [57]. This large stress relaxation may be causing the lattice parameter to appear larger than usual. Although there is no tempering involved in the current study, the samples are kept at room temperature after cryogenic treatment. The *c*/*a* ratio of cryogenically treated and tempered steel may be higher or lower than conventionally quenched and tempered steel, depending on the composition and tempering temperature [55]. So the increase in interstitial carbon of cryogenically treated samples observed in 4.5c and 4.5d might be an effect of increased *c*/*a* ratio at room temperature.

An interesting observation is that although the dislocation density and weight% carbon in interstitials seem to increase more for mid-size PAGS, the hardness increase in both LC and HC after cryogenic treatment is almost uniform, as shown in figure 3.14. One reason might be that carbon clustering due to cryogenic treatment might have resulted in formation of very fine carbides, after being kept at room temperature. Such phenomena is very commonly observed after cryogenic treatment and tempering of tool steels [58, 59]. Also, is observed that there is a weak but direct correlation between increasing dislocation density and interstitial carbon for mid-sized PAG samples after cryogenic treatment. The reason for this may be that at cryogenic temperatures,

carbon mobility is seriously hampered, as a result carbon atoms are unable to move to dislocations and remain at the interstitial sites.

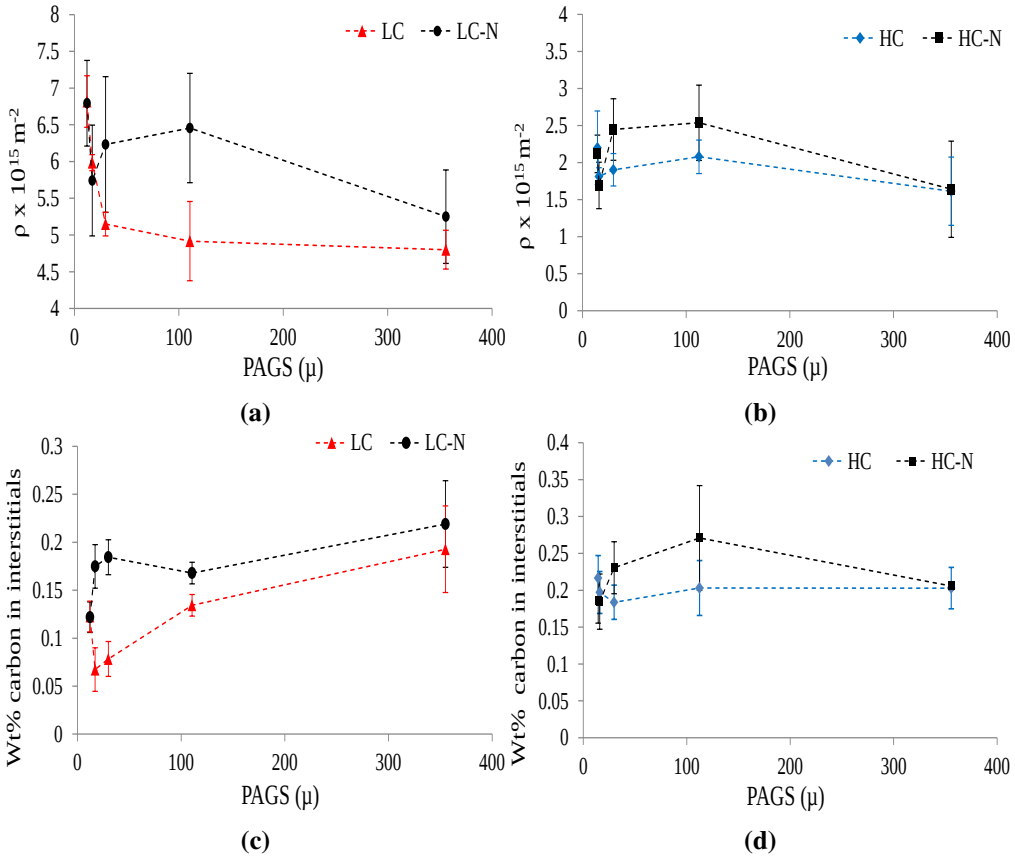


**Figure 4.5:** Variation of dislocation density (a, b) and weight% C in interstitial (c, d) vs PAGS in LC, LC-N and HC, HC-N samples

## 4.6 Comments on Uncertainties in Measurements

It is to be kept in mind that even after taking necessary precautions, some errors might creep in during measurements. The values of dislocation density and lattice parameters calculated using XRD measurements contain errors. This is because the method employed to calculate these quantities require obtaining some good linear fits from the data. Slope or intercept of such fits is then used in further calculations. Even a small error in these quantities ends up giving considerable error in the final calculations. The method used to calculate dislocation density in HC samples where average FWHM values of the diffracted martensite split peaks were taken, is not an established one. However, it gives good required fits in the plots of modified-Williamson-Hall method and provides us values using which a comparative analysis can be made. Also, there may be some effect of residual stress relaxation on retained austenite too, since apparently the fraction of retained austenite after cryogenic treatment is still high. This could affect the reasoning for observed increase in hardness after cryogenic treatment.

# Chapter 5

# Conclusions

The role of carbon in strengthening mechanisms of martensitic steels was studied. Alloys with following composition in wt.% were selected: 0.3C-3.6Mn-1.5Si and 0.6C-3.5Mn-1.5Si. The conclusions derived from the results are:

- Upon increasing austenitization temperature, the prior austenite grain size (PAGS) increases in both alloys studied. Increase in PAGS further leads to an increase in $M_S$ temperature upon quenching. This increase in $M_S$ temperature is more pronounced in alloy with 0.3 wt.% C. It shows that the prior austenite strengthening by dislocations is more sensitive to PAGS when total carbon content is lower.
- In alloy with 0.3 wt.% C, the higher the PAGS, the more is the carbon remaining at interstitial sites. But in alloy with 0.6 wt.% C, carbon concentration at interstitial sites remains nearly same irrespective of the PAGS.
- The most important factor controlling the distribution of carbon inside martensite and influencing other strengthening mechanisms is the martensite dislocation density. The extent of its influence depends upon PAGS and alloy composition.
- Martensite dislocation density, $\rho$, influences some other strengthening mechanisms too. If $\rho$ does not show any trend with varying PAGS, then other strengthening mechanisms also do not show any significant trend with varying PAGS.
- The increased hardness of cryogenically treated LC-N and HC-N samples is most probably a result of carbon clustering at cryogenic temperature and subsequent formation of very fine carbides at room temperature.
- The modified Williamson-Hall method to calculate dislocation density cannot be directly applied to carbon steels which have high tetragonality. In this work, a new method is proposed to incorporate the tetragonality of the material into the modified Williamson-Hall method.

# Chapter 6

# Recommendations for Future Work

- As evident from this work, the dislocation density is the main controlling factor behind various strengthening mechanisms and its dependence on PAGS appears to be composition dependent. Therefore, extensive investigation of dependence of martensite dislocation density on PAGS for various alloy compositions is needed.
- The carbide precipitates formed in martensite due to autotempering become coarser with increasing PAGS. Proper study is needed to make sure if this can be taken as an evidence of increasing volume fraction of carbides with increasing PAGS by providing quantitative evidence.
- The dislocation density and carbon content in interstitials calculated from the results of XRD measurements contain considerable errors. Similar study should ideally be repeated with experimental techniques which give more accurate measurements, such as TEM, APT, etc.
- The modified Williamson-Hall method used for calculation of dislocation density gives poor results for carbon steels where there is considerable tetragonality to cause peak splitting in XRD. A workaround is used in this work, for which the accuracy is needed to be checked by comparing with measurements from more accurate techniques.
- Tensile tests can be performed in order to check whether tensile strength follows the same trend with PAGS as hardness.

# Bibliography


[1] James Moore Swank. *History of the Manufacture of Iron in All Ages*. 1892.

[2] World Steel Association. Steel facts. https://www.worldsteel.org/media-centre/about-steel/steel-facts.html.

[3] Hassan Ghassemi-Armaki, Peng Chen, Shrikant Bhat, Sriram Sadagopan, Sharvan Kumar, and Allan Bower. Microscale-calibrated modeling of the deformation response of low-carbon martensite. *Journal of Alloys and Compounds*, 61:3640–3652, 2013.

[4] George Krauss. Martensite in steel: strength and structure. *Material Science and Engineering*, 273-275:40–57, 1999.

[5] Bevis Hutchinson, Joacim Hagstrom, Oskar Karlsson, David Lindell, and Malin Tornberg. Microstructures and hardness of as-quenched martensites (0.1-0.5% C). *Scripta Metallurgica*, 59:5845–5858, 2011.

[6] Willian D. Callister. *Material Science and Engineering: An Introduction*. 2006.

[7] Manfred Ahlers. The martensitic transformation. *Proceedings of Physical Society*, 9:169–183, 2004.

[8] W.Y. Zhang, J.P. Ge, H. Gong, and X.M. Zhang. The variations of martensitic morphology and habit plane in high carbon stee1. *JOURNAL DE PHYSIQUE IV*, 5, 1995.

[9] T. Maki. Microstructure and mechanical behavior of ferrous martensite. *Materials Science Forums*, 56-58:157–168, 1990.

[10] Flake C. Campbell. *Elements of Metallurgy and Engineering Alloys*. ASM International, 2008.

[11] John D. Verhoeven. *Fundamentals of Physical Metallurgy*, chapter 13. Wiley, 1975.

[12] Hiromoto Kitahara, Rintaro Ueji, Nobuhiro Tsuji, and Yoritoshi Minamino. Crystallographic features of lath martensite in low-carbon steel. *Acta Materialia*, 54:1279–1288, 2006.

[13] Javier Hidalgo and Maria Jesus Santofimia. Effect of prior austenite grain size refinement by thermal cycling on the microstructural features of as-quenched lath martensite. *Metall and Mat Trans A*, 47:5288–5302, 2015.

[14] Farideh Hajy Akbary, Jilt Sietsma, Amarante J.Böttger, and Maria J.Santofimia. An improved x-ray diffraction analysis method to characterize dis-location density in lath martensitic structures. *Materials Science & Engineering A*, 639:208–218, 2015.

[15] E.I. Galindo-Nava and P.E.J. Rivera-Diaz del Castillo. Understanding the factors controlling the hardness in martensitic steels. *Scripta Materialia*, 110:96–100, 2016.

[16] S. Morito, H. Yoshida, T. Maki, and X. Huang. Effect of block size on the strength of lath martensite in low carbon steels martensite. *Material Science and Engineering A*, 438-440:237–240, 2006.

[17] E.O. Hall. The deformation and ageing of mild steel: I11 discussion of results. *Proceedings of Physical Society*, 64:747–753, 1951.

[18] T. Gladman. Precipitation hardening in metals. *Materials Science and Technology*, 15:30–36, 1999.

[19] R.G. Speich and H.Warlimont. Yield strength and transformation substructure of low carbon martensite. *J. Iron and Steel Inst.*, 206:385–392, 1968.

[20] M. Kehoe and P.M. Kelly. The role of carbon in the strength of ferrous martensite. *Scripta Metallurgica*, 4:473–476, 1970.

[21] J.J. Hoyos, A.A. Ghiralducci, and D. Mari. Evaluation of dislocation density and interstitial carbon content in quenched and tempered steel by internal friction. *Material Science and Engineering A*, 640:460–464, 2015.

[22] Ji Dong, Chenxi Liu, Yongchang Liu, Chong Li, Qianying Guo, and Huijun Li. Influence of austenite grain size on martensite start temperature of nb-v-ti microalloyed ultra-high strength steel. *Materials Science Forum*, 848:624–632, 2016.

[23] Rui Zhang and Richard D. Sisson Jr. The influence of temperature on the austenite grain size and microstructure of 4140 steel. *Proceedings of the 28th ASM Heat Treating Society Conference*, 2015.

[24] Y. Prawoto, N. Jasmawati, and K. Sumeru. Effect of prior austenite grain size on the morphology and mechanical properties of martensite in medium carbon steel. *J. Mater. Sci. Technol.*, 28:461–466, 2012.

[25] S.C Kennett, G. Krauss, and K.O. Findley. Prior austenite grain size and tempering effects on the dislocation density of low-c nb-ti microalloyed lath martensite. *Scripta Materialia*, 107:123–126, 2015.

[26] Toshihiro Hanamura, Shiro Torizuka, Soutaro Tamura, Shohei Enokida, and Hiroshi Takechi. Effect of austenite grain size on transformation behavior, microstructure and mechanical properties of 0.1C-5mn martensitic steel. *ISIJ International*, 53:123–126, 2013.

[27] Andre Barros Cota, Fernando Lucas Gonzalves e Oliveira, Anderson Luiz da Rocha e Barbosa, Cassio Antonio Mendes Lacerda, and Fernando Gabriel da Silva Araujo. Microstructure and mechanical properties of a microalloyed steel after thermal treatments. *Materials Research*, 6:117–121, 2003.

[28] Z. Lu, R.G. Faulkner, N. Riddle, F.D. Martino, and K. Yang. Effect of heat treatment on microstructure and hardness of eurofer 97, eurofer ods and t92 steels. *Journal of Nuclear Materials*, 386-388:445–448, 2009.

[29] E.I. Galindo-Nava and P.E.J. Rivera-DÃaz del Castillo. A model for the microstructure behaviour and strength evolution in lath martensite. *Acta Materialia*, 98:81–93, 2015.

[30] C. Garcia de Andres, F. G. Caballero, C. Capdevila, and D. San Martin. Revealing austenite grain boundaries by thermal etching:advantages and disadvantages. *Materials Characterization*, 49:121–127, 2012.

[31] B.D. Cullity and S.R. Stock. *Elements of X-Ray Diffraction*. Pearson, 2014.

[32] T. Ungar and A. Borbely. The effect of dislocation contrast on x-ray line broadening: A new approach to line profile analysis. *Appl. Phys. Lett.*, 69:3173, 1996.

[33] T. Ungar, I. Dragomir, A. Revesz, and A. Borbely. The contrast factors of dislocations in cubic crystals: the dislocation model of strain anisotropy in practice. *J. Appl. Cryst.*, 32:992–1002, 1999.

[34] Sudook A. Kim and Ward L. Johnson. Elastic constants and internal friction of martensitic steel, ferritic-pearlitic steel, and α iron. *Materials Science and Engineering A*, 452-453:633–639, 2007.

[35] T. Ungar and G. Tichy. The effect of dislocation contrast on x-ray line profiles in untextured polycrystals. *phys. stat. sol. (a)*, 171:425–434, 1999.

[36] Liu Xiao, Zhong Fan, and Zhang Jinxiu. Lattice-parameter variation with carbon content of martensite. i. x-ray-diffraction experimental study. *PHYSICAL REVIEW B*, 52, 1995.

[37] N.N. Rammoa. A model for the prediction of lattice parameters of iron-carbon austenite and martensite. *Journal of Alloys and Compounds*, 420:117–120, 2006.

[38] Yang-Yu Su, Liu-Ho Chiu, Tao-Liang Chuang, Chien-Lung Huang, Cheng-Yen Wu, and Kuan-Chueh Liao. Retained austenite amount determination comparison in jis skd11 steel using quantitative metallography and x-ray diffraction methods. *Advanced Materials Research*, 482-484:1165–1168, 2012.

[39] Chester F. Jatczak. Retained austenite and its measurement by x-ray diffraction. 1980.

[40] N. H. van Dijk, A. M. Butt, L. Zhao, J. Sietsma, S. E. Offerman, J. P. Wright, and S. van der Zwaag. Thermal stability of retained austenite in trip steels studied by synchrotron x-ray diffraction during cooling. *Acta Materialia*, 53:5439–5447, 2005.

[41] J. TRZASKA. Calculation of critical temperatures by empirical formulae. *Arch. Metall. Mater.*, 61:981–986, 2016.

[42] Hong-Seok Yang and H. K. D. H. Bhadeshia. Uncertainties in dilatometric determination of martensite start temperature. *Materials Science and Technology*, 23:556–560, 2007.

[43] S. W. Ooi1, Y. R. Cho, J. K. Oh, and H. K. D. H. Bhadeshia. Carbon enrichment in residual austenite during martensitic transformation, 2015.

[44] George Krauss. *Steels: Processing, Structure and Performance*. ASM International, 2005.

[45] Carlos Capdevila, Francisca G. Caballero, and Carlos GarcÃa de AndrÃ©s. Analysis of effect of alloying elements on martensite start temperature of steels. *Materials Science and Technology*, 19, 2003.

[46] SEOK-JAE LEE and KYONG-SU PARK. Prediction of martensite start temperature in alloy steels with different grain sizes. *METALLURGICAL AND MATERIALS TRANSACTIONS A*, 44A:3423–3427, 2013.

[47] K.W. Andrews. Empirical formulae for the calculation of some transformation temperatures. *Journal of the Iron and Steel Institute*, 203:721–727, 1965.

[48] S.M.C. van Bohemen and L. Morsdorf b. Predicting the ms temperature of steels with a thermodynamic based model including the effect of the prior austenite grain size. *Acta Materialia*, 125:401–415, 2017.

[49] T Sourmail and V Smanio. Determination of $m_s$ temperature: methods, meaning and influence of 'slow start' phenomenon. *Materials Science and Technology*, 29:883–888, 2013.

[50] T. Furuhara, S. Morito, and T. Maki. Morphology, substructure and crystallography of lath martensite in fe-c alloys. *J. Phys. IV France*, 112:255–258, 2003.

[51] L. Morsdorf, C.C. Tasan, D. Ponge, and D. Raabe. 3d structural and atomic-scale analysis of lath martensite: Effect of the transformation sequence. *Acta Materialia*, 95:366–377, 2015.

[52] S. W. Ooi, Y. R. Cho, J. K. Oh, and H. K. D. H. Bhadeshia. Carbon enrichment in residual austenite during martensitic transformation. *ICOMAT-2008*, 2009.

[53] Akinobu Shibata, Takashi Nagoshi, Masato Sone, Shigekazu Morito, and Yakichi Higo. Evaluation of the block boundary and sub-block boundary strengths of ferrous lath martensite using a micro-bending test. *Materials Science & Engineering A*, 527:7538–7544, 2010.

[54] Thomas Simm, Lin Sun, Steven McAdam, Paul Hill, Martin Rawson, and Karen Perkins. The influence of lath, block and prior austenite grain (pag) size on the tensile, creep and fatigue properties of novel maraging steel. *Materials*, 10, 2017.

[55] Yang-Yu Su, Liu-Ho Chiu, Fan-Shiong Chen, Shou-Chi Lin, and Yeong-Tsuen Pan. Residual stresses and dimensional changes related to the lattice parameter changes of heat-treated jis skd 11 tool steels. *Materials Transactions*, 55:241–244, 2014.

[56] J.Y. Huang, Y.T. Zhu, X.Z. Liao, I.J. Beyerlein, M.A. Bourke, and T.E. Mitchell. Microstructure of cryogenic treated m2 tool steel. *Materials Science and Engineering A*, 339:241–244, 2003.

[57] A. Bensely, S. Venkatesh, D. Mohan Lal, G. Nagarajan, A. Rajadurai, and Krzysztof Junik. Effect of cryogenic treatment on distribution of residual stress in case carburized en 353 steel. *Materials Science and Engineering A*, 479:229–235, 2008.

[58] C C Wu, W C Chen, and L H Chen. Effects of cryogenic treatment on mechanical property and microstructure of jis skh51 high-speed steel. *IOP Conf. Series: Materials Science and Engineering*, 103, 2015.

[59] Hadi Ghasemi-Nanesa and Mohammad Jahazi. Simultaneous enhancement of strength and ductility in cryogenically treated AISI D2 tool steel. *Materials Science & Engineering A*, 598:413–419, 2014.